https://doi.org/10.5194/amt-2022-143
Preprint. Discussion started: 29 June 2022

Atmospheric Measurement Techniques Discussions
Open Access
EGU

The Education and Research 3D Radiative Transfer Toolbox (EaR^{3}T) – Towards the Mitigation of 3D Bias in Airborne and Spaceborne Passive Imagery Cloud Retrievals

Hong Chen[1,2], K. Sebastian Schmidt[1,2], Steven T. Massie[2], Vikas Nataraja[2], Matthew S. Norgren[2], Jake J. Gristey[3,4], Graham Feingold[4], Robert E. Holz[5], Hironobu Iwabuchi[6]

[1]Department of Atmospheric and Oceanic Sciences, University of Colorado, Boulder, CO, USA
[2]Laboratory for Atmospheric and Space Physics, University of Colorado, Boulder, CO, USA
[3]Cooperative Institute for Research in Environmental Sciences, University of Colorado, Boulder, CO, USA
[4]NOAA Chemical Sciences Laboratory, Boulder, CO, USA
[5]Space Science and Engineering Center, University of Wisconsin–Madison, Madison, WI, USA
[6]Center for Atmospheric and Oceanic Studies, Tohoku University, Sendai, Miyagi, Japan

Correspondence to: Hong Chen (hong.chen-1@colorado.edu)

https://doi.org/10.5194/amt-2022-143
Preprint. Discussion started: 29 June 2022

Atmospheric Measurement Techniques Discussions

Abstract

We introduce the Education and Research 3D Radiative Transfer Toolbox (EaR^{3}T) for quantifying and mitigating artifacts in atmospheric radiation science algorithms due to spatially inhomogeneous clouds and surfaces, and show the benefits of automated, realistic radiance and irradiance generation along extended satellite orbits, flight tracks from entire aircraft field missions, and synthetic data generation from model data. EaR^{3}T is a modularized Python package that provides high-level interfaces to automate the process of 3D radiative transfer (RT) calculations. After introducing the package, we present initial findings from four applications, which are intended as blueprints to future in-depth scientific studies. The first two applications use EaR^{3}T as a satellite radiance simulator for the NASA OCO-2 and MODIS missions, which generate synthetic satellite observations with 3D-RT on the basis of cloud field properties from imagery-based retrievals and other input data. In the case of inhomogeneous cloud fields, we show that the synthetic radiances are often inconsistent with the original radiance measurements. This lack of radiance consistency points to biases in heritage imagery cloud retrievals due to sub-pixel resolution clouds and 3D-RT effects. They come to light because the simulator's 3D-RT engine replicates processes in nature that conventional 1D-RT retrievals do not capture. We argue that 3D radiance consistency (closure) can serve as a metric for assessing the performance of a cloud retrieval in presence of spatial cloud inhomogeneity even with limited independent validation data. The other two applications show how airborne measured irradiance data can be used to independently validate imagery-derived cloud products via radiative closure in irradiance. This is accomplished by simulating downwelling irradiance from geostationary cloud retrievals of Advanced Himawari Imager (AHI) along all the below-cloud aircraft flight tracks of the Cloud, Aerosol and Monsoon Processes Philippines Experiment (CAMP^{2}Ex, NASA 2019), and comparing the irradiances with the collocated airborne measurements. In contrast to isolated case studies in the past, EaR^{3}T facilitates the use of observations from entire field campaigns for the statistical validation of satellite-derived irradiance. From the CAMP^{2}Ex mission, we find a low bias of 10% in the satellite-derived cloud transmittance, which we are able to attribute to a combination of the coarse resolution of the geostationary imager and 3D-RT biases. Finally, we apply a recently developed context-aware CNN cloud retrieval framework to high-resolution airborne imagery from CAMP^{2}Ex and show that the retrieved cloud optical thickness fields lead to better 3D radiance consistency than the heritage independent pixel algorithm, opening the door to future mitigation of 3D-RT cloud retrieval biases.

https://doi.org/10.5194/amt-2022-143
Preprint. Discussion started: 29 June 2022

Atmospheric Measurement Techniques Discussions

1. Introduction

Three-dimensional cloud effects in imagery-derived cloud properties have long been considered an unavoidable error source when estimating the radiative effect of clouds and aerosols. Consequently, research efforts involving satellite, aircraft, and surface observations in conjunction with modeled clouds and radiative transfer calculations have focused on systematic bias quantification under different atmospheric conditions. Barker and Liu (1995) studied the so-called independent pixel approximation (IPA) bias in cloud optical thickness (COT) retrievals from shortwave cloud reflectance. The bias arises when approximating the radiative transfer relating to COT and measured reflectance at the pixel or cloud column level through one-dimensional (1D) radiative transfer (RT) calculations, while ignoring its radiative context. However, net horizontal photon transport and other effects such as shading engender column-to-column radiative interactions that can only be captured in a three-dimensional (3D) framework, and can be regarded as a 3D perturbation or bias relative to the 1D-RT (IPA) baseline. 3D biases affect not only cloud remote sensing but they also propagate into the derived irradiance fields and cloud radiative effects (CRE). Since the derivation of regional and global CRE relies heavily on satellite imagery, any systematic 3D bias impacts the accuracy of the Earth's radiative budget. Likewise, imagery-based aerosol remote sensing in the vicinity of clouds can be biased by net horizontal photon transport (Marshak et al., 2008). Additionally, satellite shortwave spectroscopy retrievals of CO_2 mixing ratio are affected by nearby clouds (Massie et al., 2017), albeit through a different physical mechanism than in aerosol and cloud remote sensing (Schmidt et al., 2022).

Given the importance of 3D perturbations for atmospheric remote sensing, ongoing research seeks to mitigate the 3D effects. Cloud tomography, for example, inverts multi-angle radiances to infer the 3D cloud extinction distribution (Levis et al., 2020). This is achieved through iterative adjustments to the cloud field until the calculated radiances match the observations. Convolutional neural networks (CNNs, Masuda et al., 2019; Nataraja et al., 2022) account for 3D-RT perturbations in COT retrievals through pattern-based machine learning that operates on collections of imagery pixels, rather than treating them in isolation like IPA. Unlike tomography, CNNs require training based on extensive cloud-type specific synthetic data with the ground truth of cloud optical properties and their associated radiances from 3D-RT calculations. Once the CNNs are trained, they do not require real-time 3D-RT calculations and can therefore be useful in an operational setting. Whatever the future may hold for context-aware multi-pixel or multi-sensor

Atmospheric Measurement Techniques Discussions

cloud retrievals, there is a paradigm shift on the horizon that started when the radiation concept for the Earth Clouds, Aerosol and Radiation Explorer (EarthCARE, Illingworth et al., 2015) was first proposed (Barker et al., 2012). It foresees a closure loop where broadband radiances, along with irradiance, are calculated in a 3D-RT framework from multi-sensor input fields (Barker et al., 2011), and subsequently compared to independent observations by radiometers pointing in three directions (nadir, forward-, and backward-viewing along the orbit). This built-in radiance closure can serve as an accuracy metric for any downstream radiation products such as heating rates and CRE. Any inconsistencies can be used to nudge the input fields towards the truth in subsequent loop iterations akin to optimal estimation, or propagated into uncertainties of the cloud and radiation products.

This general approach to radiative closure is also being considered for the National Aeronautics and Space Administration (NASA) Atmospheric Observation System (AOS, developed under the A-CCP, Aerosol and Cloud, Convection and Precipitation study), a mission that is currently in its early implementation stages. Owing to its focus on studying aerosol-cloud-precipitation-radiation interactions at the process level, it requires radiation observables at a finer spatial resolution than achieved with missions to date. At target scales close to 1 km, 3D-RT effects are much more pronounced than at the traditional 20 km scale of NASA radiation products (O'Hirok and Gautier, 2005; Ham et al., 2014; Song et al., 2016; Gristey et al., 2020a). Since this leads to biases beyond the desired accuracy of the radiation products, mitigation of 3D-RT cloud remote sensing biases needs to be actively pursued over the next few years.

Transitioning to an explicit treatment of 3D-RT in operational approaches entails a new generation of code architectures that can be easily configured for various instrument constellations, interlink remote sensing parameters with irradiances, heating rates, and other radiative effects, and can be used for automated processing of large data quantities.

Here, we introduce one such tool that could serve as the seed for this transition: the Education and Research 3D Radiative Transfer Toolbox (EaR^{3}T). It has been developed over the past few years at the University of Colorado to automate 3D-RT calculations based on imagery or model cloud fields with minimal user input. EaR^{3}T is maintained and extended by graduate students as part of their education, and applied to various different research projects including machine learning for atmospheric radiation and remote sensing (Gristey et al., 2020b; 2022; Nataraja et al., 2022), as well as radiative closure and satellite simulators (this paper and Schmidt et al., 2022). It is implemented as a modularized Python package with various application codes that combine the functionality in different ways.

The goal of the paper is to introduce EaR^{3}T as a versatile tool for systematically quantifying the mitigating 3D cloud effects in radiation science as foreseen in future missions. To do so, we will first showcase EaR^{3}T as an automated radiance simulator for two satellite instruments, the Orbiting Carbon Observatory-2 (OCO-2, this application is referred to as APP1 in this manuscript) and the Moderate Resolution Imaging Spectroradiometer (MODIS, application code 2, APP2) from publicly available satellite retrieval products. In the spirit of radiance closure, the intended use is the comparison of modeled radiances with the original measurements to assess the accuracy of the input data, as follows: operational IPA COT products are made using 1D-RT, and thus the accompanying radiances are consistent with the original measurements under that 1D-RT assumption only. That is, self-consistency is assured if 1D-RT is used in both the inversion and radiance simulation. However, since nature operates on 3D-RT, we break this traditional symmetry in this manuscript and introduce the concept of 3D radiance consistency where closure is only achieved if the original measurements are consistent with the 3D-RT (rather than the 1D-RT) simulations. The level of inconsistency is then used as a metric for the magnitude of 3D-RT retrieval artifacts as envisioned by the architects of the EarthCARE radiation concept (Barker et al., 2012).

Subsequently, we discuss applications where EaR^{3}T performs radiative closure in the traditional sense, i.e., between irradiances derived from satellite products and collocated airborne or ground-based observations. The aircraft Cloud, Aerosol and Monsoon Processes Philippines Experiment (CAMP^{2}Ex, Reid et al., 2022), conducted by NASA in the Philippines in 2019, serves as a testbed of this approach. Here, we use EaR^{3}T's automated processing capabilities to derive irradiance from geostationary imagery cloud products and then compare these to cumulative measurements made along all flight legs of the campaign (application code 3, APP3). In contrast to previous studies that often rely on a number of cases (e.g., Schmidt et al., 2010; Kindel et al., 2010), we perform closure systematically for the entire data set, enabling us to identify 3D-RT biases in a statistically significant manner. Finally, we apply a regionally and cloud type specific CNN, introduced by Nataraja et al. (2022) that is included with the EaR^{3}T distribution, to high-resolution camera imagery from CAMP^{2}Ex. This last example demonstrates mitigation of 3D-RT

https://doi.org/10.5194/amt-2022-143
Preprint. Discussion started: 29 June 2022

Atmospheric Measurement Techniques Discussions
Open Access
EGU

biases in cloud retrievals using the concept of radiance closure to quantify its performance against the baseline IPA (application code 4).

The general concept of EaR^{3}T with an overview of the applications, along with the data used for both parts of the paper is presented in section 2, followed by a description of the procedures of EaR^{3}T in section 3. Results for the OCO-2 and MODIS satellite simulators (part 1) are shown in section 4, followed by the quantification and mitigation of 3D-RT biases with CAMP^{2}Ex data in section 5 and section 6 (part 2). A summary and conclusion are provided in section 7. The code, along with the applications presented in this paper, can be downloaded from the github repository: https://github.com/hong-chen/er3t.

2. Functionality and Data Flow within EaR^{3}T

2.1 Overview

To introduce EaR^{3}T as a satellite radiance simulator tool and to demonstrate its use for the quantification and mitigation of 3D cloud remote sensing biases, five applications (Figure 1) are included in the github software release, four of which are discussed in this paper:

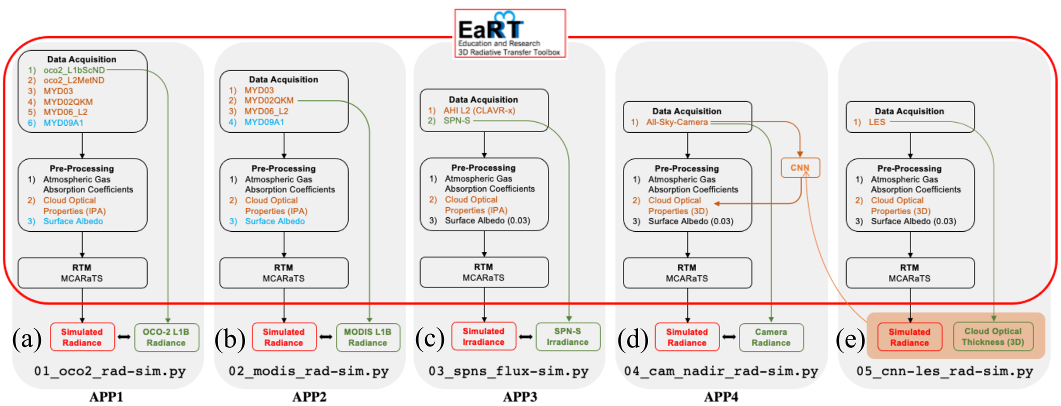

Figure 1. Flow charts of EaR^{3}T applications for (a) OCO-2 radiance simulation at 768.52 nm (data described in section 2.2.1 and 2.2.2, results discussed in section 4), (b) MODIS radiance simulation at 650 nm (data described in section 2.2.1, results discussed in section 4), (c) SPN-S irradiance simulation at 745 nm (data described in section 2.2.3 and 2.2.4, results discussed in section 5), (d) all-sky camera radiance simulation at 600 nm (data described in section 2.2.5, results discussed in section 6), and (e) radiance simulation at 600 nm based on LES data for CNN training (not included in this paper). The data products and their abbreviations are described in section 2.2.

https://doi.org/10.5194/amt-2022-143
Preprint. Discussion started: 29 June 2022

Atmospheric Measurement Techniques Discussions

1. APP1, section 4.1 (`examples/01_oco2_rad-sim.py`): Radiance simulations along the track of OCO-2 , based on data products from MODIS and others – to assess consistency (closure) between simulated and measured radiance;
2. APP2, section 4.2 (`examples/02_modis_rad-sim.py`): MODIS radiance simulations – to assess self-consistency of MODIS level-2 (L2) products with the associated radiance fields (L1B product) under spatially inhomogeneous conditions;
3. APP3, section 5 (`examples/03_spns_flux-sim.py`): Irradiance simulations along aircraft flight tracks, utilizing the L2 cloud products of the AHI , and comparison with aircraft measurements – to quantify retrieval biases due to 3D cloud structure based with data from an entire aircraft field campaign;
4. APP4, section 6 (`examples/04_cam_nadir_rad-sim.py`): Mitigation of 3D cloud biases in passive imagery COT retrievals from an airborne camera, application of a convolutional neural network (CNN) and subsequent comparison of CNN-derived radiances with the original measurements – to illustrate how the radiance self-consistency concept assesses the fidelity of cloud retrievals.

Figure 1 shows the high-level workflow of the applications. The first four share the general concept of evaluating simulations (the output from the EaR^{3}T, indicated in red at the bottom of each column) with observations (indicated in green at the bottom) from various satellite and aircraft instruments. The results for the four applications are interpreted in section 4.1, section 4.2, section 5, and section 6. The workflow of each application consists of three parts – 1) data acquisition, 2) pre-processing, and 3) RTM setup and execution. EaR^{3}T includes functions to ingest data from various different sources, e.g., satellite data from publicly available data archives, which can be combined in different ways to accommodate input data depending on the application specifics. For example, in APP1, EaR^{3}T is used to automatically download and process MODIS and OCO-2 data files based on the user-specified region, date and time. Building on the templates provided in the current code distribution, the functionality can be extended to new spaceborne or airborne instruments. The fifth column of Figure 1 shows an application that differs from the first four, and was developed for earlier papers (Gristey et al., 2020a and 2020b; Nataraja et al., 2022; Gristey et al., 2022). In contrast to the first four, which use imagery products as input, the fifth application ingests model output from a Large Eddy Simulation (LES) and produces irradiance data for surface energy budget applications, or synthetic radiance fields for training a CNN. Details

https://doi.org/10.5194/amt-2022-143
Preprint. Discussion started: 29 June 2022

Atmospheric Measurement Techniques Discussions

and results are described in the respective papers. Furthermore, Schmidt et al. (2022) builds upon APP1 to study the mechanism of 3D cloud biases in OCO-2 passive spectroscopy retrievals.

After the required data files have been downloaded in the data acquisition step, EaR^{3}T pre-processes them and generates the optical properties of atmospheric gases, clouds, aerosols, and the surface. In Figure 1, the mapping from input data to these properties is color-coded component-wise (brown for associated cloud property processing if available, blue for associated surface property processing if available, green for associated ground truth property). Although the current version only includes Monte Carlo Atmospheric Radiative Transfer Simulator (MCARaTS, Iwabuchi, 2006) as the 3D RT solver, EaR^{3}T is designed to be modular so as to employ various different solvers. To achieve this flexibility, pre-processing is a required intermediate step since different RT solvers interface with the input data differently. Although the four applications included in this paper do not take aerosol layers into consideration, the setup of processing optical properties for aerosols is supported and has been used in other applications, such as studying cloud-aerosol radiative effects based on LES data (Gristey et al., 2022). After pre-processing, the optical properties are fed into the RT solver. Finally, the user obtains radiation output from EaR^{3}T, either radiance or irradiance. The output is saved in HDF5 format and can be easily distributed and accessed by various programming languages. The data variables contained in the HDF5 output are provided in Table 1.

Metadata			
Variable Name	Description	Data Type	Dimension
`mean/N_photon`	Number of photons per run	Array	N_g
`mean/N_run`	Number of runs	Integer value	N/A
`mean/toa`	TOA downwelling flux	Float value	N/A
Radiance			
Variable Name	Description	Data Type	Dimension
`mean/rad`	Radiance field at user specified altitude averaged over different runs	Array	(N_x, N_y)
`mean/rad_std`	Standard deviation of the radiance	Array	(N_x, N_y)

	fields from different runs		
Irradiance			
Variable Name	Description	Data Type	Dimension
`mean/f_down`	Downwelling irradiance averaged over different runs	Array	(N_x, N_y, N_z)
`mean/f_down_std`	Standard deviation of the downwelling irradiance from different runs	Array	(N_x, N_y, N_z)
`mean/f_down_diffuse`	Diffuse downwelling irradiance averaged over different runs	Array	(N_x, N_y, N_z)
`mean/f_down_diffuse_std`	Standard deviation of the diffuse downwelling irradiance from different runs	Array	(N_x, N_y, N_z)
`mean/f_down_direct`	Direct downwelling irradiance averaged over different runs	Array	(N_x, N_y, N_z)
`mean/f_down_direct_std`	Standard deviation of the direct downwelling irradiance from different runs	Array	(N_x, N_y, N_z)
`mean/f_up`	Upwelling irradiance averaged over different runs	Array	(N_x, N_y, N_z)
`mean/f_up_std`	Standard deviation of the upwelling irradiance from different runs	Array	(N_x, N_y, N_z)

Table 1: Data variables contained in the output HDF5 file from EaR^{3}T for radiance and irradiance calculations. The radiance is simulated with a user-specified sensor geometry at a given altitude using forward photon tracing. The data variables listed under Metadata are included for both radiance and irradiance calculations. N_x, N_y, and N_z are the number of pixels along x, y, and z direction, respectively. N_g is the number of g, explained in section 3.

https://doi.org/10.5194/amt-2022-143
Preprint. Discussion started: 29 June 2022

The aforementioned three steps – data acquisition, pre-processing, and RTM setup and execution are automated such that the 3D/1D-RT calculations can be performed for any region at any date and time using satellite or aircraft data or other data resources such as LES. EaR^{3}T is hosted on Github at https://www.github.com/hong-chen/er3t. Since it is developed as an educational and research 3D-RT tool collection by students, it is a living code base, intended to be updated over time. The master code modules for the four applications as listed in Figure 1 are included in the EaR^{3}T package under the `examples` directory.

2.2 Data

The radiance simulations in APP1 and APP2 use data from the OCO-2 and MODIS-Aqua instruments, both of which are in a sun-synchronous polar orbit with an early-afternoon equator crossing time within NASA's A-Train satellite constellation. Figure 2 visualizes radiance measurements by OCO-2 in the context of MODIS Aqua imagery over a partially vegetated and partially cloud-covered land, illustrating that MODIS provides imagery and scene context for OCO-2, which in turn observes radiances from a narrow swath. The region is located in southwest Colorado in the United States of America. We selected this case because both the surface and clouds are varied along with diverse surface types. The surface features green forest and brown soil, whereas clouds include small cumulus and large cumulonimbus. In addition, this scene contains relatively homogeneous cloud fields in the north and inhomogeneous cloud fields in the south, which allows us to evaluate the simulations from various aspects of cloud morphology. To simulate the radiances of both instruments we use data products from OCO-2 and MODIS, as well as reanalysis products from NASA's Global Modeling and Assimilation Office (GMAO) sampled at OCO-2 footprints and distributed along with OCO-2 data (section 2.2.2).

https://doi.org/10.5194/amt-2022-143
Preprint. Discussion started: 29 June 2022

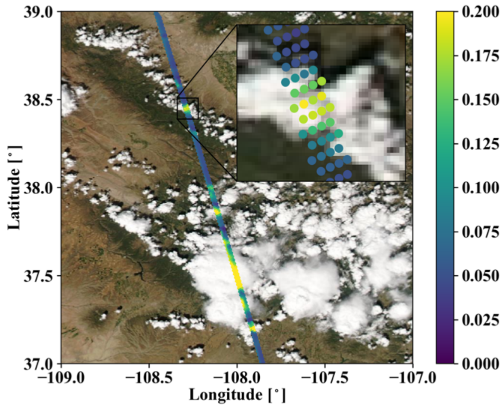

Figure 2. OCO-2 measured radiance (units: $Wm^{-2}nm^{-1}sr^{-1}$) at 768.52 nm, overlaid on MODIS Aqua RGB imagery over southwestern Colorado (USA) on 2 September, 2019. The inset shows an enlarged portion along the track, illustrating that OCO-2 radiances co-vary with MODIS-Aqua radiance observations.

For APP3 (irradiance simulations and 3D cloud bias quantification), we use geostationary imagery from the Japanese Space Agency's Advanced Himawari Imager to provide cloud information in the area of the flight path of the NASA CAMP^{2}Ex aircraft (Reid et al., 2022). The AHI data are used in conjunction with aircraft measurements of shortwave spectral radiation (section 2.2.4). Subsequently (APP4: 3D cloud bias mitigation), we demonstrate the concept of radiance closure under partially cloudy conditions with airborne camera imagery (section 2.2.5). The underlying cloud retrieval is based on a convolutional neural network (CNN), which is described in a related paper (Nataraja et al., 2022) in this special issue and relies on EaR^{3}T-generated synthetic radiance data based on Large Eddy Simulations (LES).

2.2.1 Moderate Resolution Imaging Spectroradiometer (MODIS)

MODIS is currently flying on NASA's Terra and Aqua satellites, launched in 1999 and 2002 respectively. They are multi-use multispectral radiometers conceived as central elements of the Earth Observing System (EOS, King and Platnick, 2018). For APP1 and APP2, EaR^{3}T ingests MODIS level 1B radiance products at the quarter kilometer scale (channels 1 and 2, MxD02QKM, where 'x' stands for 'O' in the case of MODIS on Terra, and 'Y' in the case of Aqua data), the geolocation product (MxD03), the level 2 cloud product (MxD06), and the surface reflectance product (MxD09A1). For this paper, we use only Aqua data (MYD), from data collection 6.1. All

https://doi.org/10.5194/amt-2022-143
Preprint. Discussion started: 29 June 2022

the data are publicly available, and are distributed at the LAADS (Level-1 and Atmosphere Archive & Distribution System) Distributed Active Archive Center (DAAC) by NASA's Goddard Space Flight Center.

For cloud properties in APP2, we use the MODIS cloud product (MxD06L2, collection 6.1). It provides cloud properties such as cloud optical thickness (COT), cloud effective radius (CER), cloud thermodynamic phase, cloud top height (CTH), etc. (Nakajima and King, 1990; Platnick et al., 2003). Since 3D cloud effects such as horizontal photon transport are most significant at small spatial scales (e.g., Song et al., 2016), we use the high-resolution red (650 nm) channel 1 (250 m), and derive COT directly from the reflectance in the Level-1B data (MYD02QKM) instead of using the coarser-scale operational product from MYD06. CER and CTH are sourced from MYD06 and re-gridded to 250 m. The EaR^{3}T strategy for MODIS data is similar, in principle, to the more advanced method by Deneke et al. (2021), which uses a high-resolution wide-band visible channel from geostationary imagery to up-sample narrow-band coarse-resolution channels. However, we simplified cloud detection and derivation of COT from reflectance data for the purpose of our paper by using a threshold method (Appendix A1) and the two-stream approximation (Appendix A2). In future versions of EaR^{3}T this will be upgraded to more sophisticated algorithms. A simple algorithm (Appendix B1) is used to correct for the parallax shift based on the sensor geometries and cloud heights. The cloud top height data is provided by the MODIS L2 cloud product and assuming cloud base is the same.

For the surface reflectance, we used MYD09A1, for which cloud-cleared observations are aggregated over an 8-day period (Vermote et al., 2015). This product is available on a sinusoidal grid with a spatial resolution of 500 m for MODIS band 2, and includes atmospheric correction for gas and aerosol scattering and absorption.

2.2.2 Orbiting Carbon Observatory 2 (OCO-2)

The OCO-2 satellite was inserted into NASA's A-Train constellation in 2014 and flies about 6 minutes ahead of Aqua. OCO-2 provides the column-averaged carbon dioxide (CO_2) dry-air mole fraction (XCO_2) through passive spectroscopy based on hyperspectral radiance observations in three narrow wavelength regions, the Oxygen A-Band (~0.76 micron), the weak CO_2 band (~1.60 micron), and the strong CO_2 band (~2.06 micron). As shown in the inset of Figure 2, it takes measurements in eight footprints across a narrow swath. Each of the footprints has a

https://doi.org/10.5194/amt-2022-143
Preprint. Discussion started: 29 June 2022

Atmospheric Measurement Techniques
Discussions

size around 1-2 km, and the spectra for the three bands are provided by separate, co-registered spectrometers (Crisp et al., 2015).

The OCO-2 data products of 1) Level 1B calibrated and geolocated science radiance spectra (L1bScND), 2) standard Level 2 geolocated XCO_2 retrievals results (L2StdND), 3) meteorological parameters interpolated from GMAO (L2MetND) at OCO-2 footprint location are downloaded from NASA GES DISC (Goddard Earth Science Data Archive and Information Services Center) data archive (https://oco2.gesdisc.eosdis.nasa.gov/data/OCO2_DATA). Since MODIS on Aqua overflies a scene 6 minutes after OCO-2, the clouds move with the wind over this time period. We therefore added a wind correction on top of the parallax-corrected cloud fields obtained from MODIS (section 2.2.1). This was done with the 10 m wind speed data from L2MetND (see Appendix B2). For the same scene as shown in Figure 2, Figure 3 shows (a) COT, (b) CER, and (c) CTH, all corrected for both parallax and wind effect.

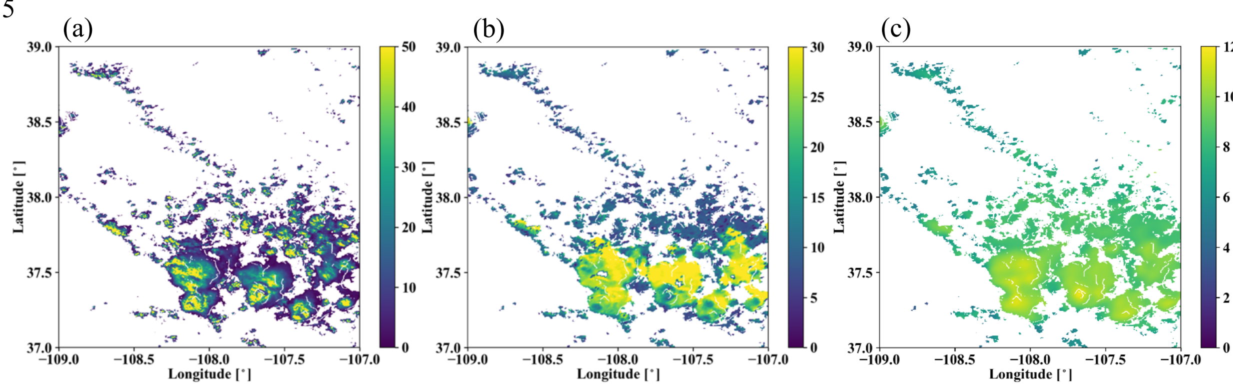

Figure 3. **(a)** Cloud optical thickness derived from MODIS L1B radiance at 650 nm by the two-stream approximation (Eq. A2), **(b)** cloud effective radius (units: μm), and **(c)** cloud top height (units: km) collocated from the MODIS L2 cloud product. The locations of the cloudy pixels were shifted to account for parallax and wind effects. The parallax correction ranged from near 0 for low clouds and 1 km for high clouds (10 km CTH). The wind correction was around 0.8 km, given the average wind speed of 2 m/s to the east.

The OCO-2 data (L2StdND) themselves only provide sparse surface reflectance for the footprints that are clear, while EaR^{3}T requires surface albedo for the whole domain. Therefore, we used MYD09A1 as a starting point. However, since MODIS does not have a channel in the Oxygen

https://doi.org/10.5194/amt-2022-143
Preprint. Discussion started: 29 June 2022

Atmospheric Measurement Techniques
Discussions

A-Band, MODIS band 2 (860 nm) was used as a proxy for the 760 nm OCO-2 channel as follows: we collocated the OCO-2 retrieved 760 nm surface reflectance R_{OCO} within the corresponding 860 nm MODIS MYD09A1 data R_{MOD} as shown in Figure 4a (same domain as Figures 2 and 3) and calculated a scaling factor assuming a linear relationship between R_{OCO} and R_{MOD} ($R_{OCO} = a \cdot R_{MOD}$). Figure 4b shows R_{OCO} versus R_{MOD} for all cloud-free OCO-2 footprints. The red line shows a linear regression (derived scale factor $a=0.93$). Scaling is also applied for the weak and strong CO_2 channels, even though there are matching MODIS channels. Optionally, the OCO-2-scaled MODIS-derived surface reflectance fields can be replaced by the OCO-2 surface reflectance products for pixels where they are available.

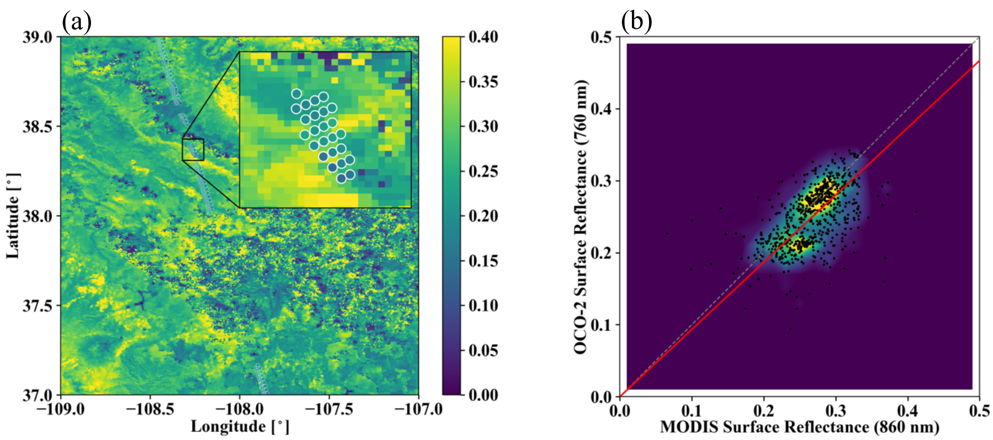

Figure 4. **(a)** Surface reflectance from the OCO-2 L2 product in the Oxygen A-band (near 760 nm), overlaid on the surface reflectance from the MODIS MYD09 product at 860 nm. **(b)** OCO-2 surface reflectance at 760 nm versus MODIS surface reflectance at 860 nm, along with linear regression ($y=ax$) as indicated by the red line (slope $a=0.9337$).

2.2.3 Advanced Himawari Imager (AHI)

The Advanced Himawari Imager (AHI, used for APP3) is a payload on Himawari-8, a geostationary satellite operated by the Meteorological Satellite Center (MSC) of the Japanese Meteorological Agency. The AHI provides 16 channels of spectral radiance measurements from the shortwave (0.47µm) to the infrared (13.3µm). During CAMP^{2}Ex, the NASA in-field

https://doi.org/10.5194/amt-2022-143
Preprint. Discussion started: 29 June 2022

Atmospheric Measurement Techniques Discussions

operational team closely collaborated with the team from MSC to provide AHI satellite imagery at the highest resolution over the Philippine Sea. From the AHI imagery, the cloud product generation system - Clouds from AVHRR Extended System (CLAVR-x), was used to generate cloud products from the AHI imagery (Heidinger et al., 2014). The cloud products from CLAVR-x include cloud optical thickness, cloud effective radius, and cloud top height at 2 (at nadir) to 5 km spatial resolution. Since AHI provides continuous regional scans every 10 minutes the AHI cloud product has a temporal resolution of 10 minutes.

2.2.4 Spectral Sunshine Pyranometer (SPN-S)

The SPN-S is a prototype spectral version of the commercially available global-diffuse SPN1 pyranometer (Wood et al., 2017; Norgren et al., 2022). The radiometer uses a 7-detector design in combination with a fixed shadow mask that enables the simultaneous measurement of both diffuse and global irradiances, from which the direct component of the global irradiance is calculated via subtraction. The detector measures spectral irradiance from 350 to 1000 nm, and the spectrum is sampled at 1 nm resolution with 1 Hz timing.

During the CAMP^{2}Ex mission, the SPN-S was mounted to the top of the NASA P-3 aircraft where it sampled downwelling solar irradiance. To ensure accurate measurements, pre- and post-mission laboratory-based calibrations were completed using tungsten "FEL" lamps that are traceable to a National Institute of Standards and Technology standard. Additionally, the direct and global irradiances were corrected for deviations of the SPN-S sensor plane from horizontal that are the result of changes in the aircraft's pitch or roll. This attitude correction applied to the irradiance data is a modified version of the method outlined in Long et al. (2010). However, whereas Long et al. (2010) employ a "box" flight pattern to characterize the sensor offset angles, in this study an aggregation of flight data containing aircraft heading changes under clear-sky conditions is used as a substitute. The estimated uncertainty of the SPN-S system is 6 to 8%, with 4 to 6% uncertainty stemming from the radiometric lamp calibration process, and up to another 2% resulting from insufficient knowledge of the sensor cosine response. The stability of the system under operating conditions is 0.5%. A thorough description of the SPN-S and its calibration and correction procedures is provided in Norgren et al. (2022). In this paper (APP3) only the global downwelling irradiance sampled by the 745 nm channel is used.

2.2.5 Airborne All-Sky Camera (ASC)

The All-Sky Camera (used for APP4) is a commercially available camera (ALCOR ALPHEA 6.0CW[1]) with fish-eye optics for hemispheric imaging. It has a Charge-Coupled Device (CCD) detector that measures radiances in red, green, and blue channels. Radiometric and geometric calibrations were performed at the Laboratory of Atmospheric and Space Physics at the University of Colorado Boulder. The three-color channels are centered at 493, 555, and 626 nm for blue, green, and red, respectively, with bandwidths of 50 – 100 nm. Only radiance data from the red channel were used in this paper. The spatial resolution of the ASC depends on the altitude of the aircraft and the viewing zenith angle. Across the hemispheric field of view of the camera, the resolution of the field angle is approximately constant, at about 0.09º. At a flight level of 5 km, this translates to a spatial resolution of 8 m at nadir. However, due to accuracy limitations of the geometric calibration and the navigational data from Inertial Navigation System (INS), the nadir geolocation accuracy could only be verified to within ±50 m. During the CAMP^{2}Ex flights, the camera exposure time was set manually to minimize saturation of the detector. The standard image frame rate is 1 Hz. The precision of the camera radiances is on the order of 1%, and the radiometric accuracy is 6 – 7%.

3. EaR^{3}T Procedures

In the previous section, we described the general workflow of EaR^{3}T applications, along with relevant data. In this section, we will focus on the specific implementation of the workflow through the EaR^{3}T software package. It is a toolbox for 3D-RT with modules for automatic input data download and processing, generation of radiative and optical properties of surface, atmospheric gases, clouds and aerosols, wrappers for 3D-RT solvers and output post-processing, with the end goal to simulate radiances and irradiances along entire satellite orbits or aircraft flight tracks. Unlike established radiative transfer packages such as libRadtran (Mayer and Kylling, 2005; Emde et al., 2016), which provide extensive libraries of optical properties along with a selection of solvers, EaR^{3}T focuses on automated radiative transfer for two- or three-dimensional cloud,

[1]https://www.alcor-system.com/common/allSky/docs/ALPHEA_Camera%20ALL%20SKY%20CAMERA_Doc.pdf last accessed on April 24, 2022.

https://doi.org/10.5194/amt-2022-143
Preprint. Discussion started: 29 June 2022

aerosol, and surface input data, and therefore only comes with minimal options for optical properties, and solvers. The initial release is available at https://github.com/hong-chen/er3t.

We will now walk through the OCO-2 and MODIS simulator applications with the codes `examples/01_oco2_rad-sim.py` (APP1) and `examples/02_modis_rad-sim.py` (APP2). The data acquisition (first step in Figure 1) uses functions in `er3t/util`. APP1 and APP2 use the functions in `er3t/util/modis.py` and `er3t/util/oco.py` for downloading the MODIS and OCO-2 data files from the respective NASA data archives and for processing the data (e.g., geo-mapping, gridding etc.). The user supplies minimum input (date and time, as well as latitudes and longitudes of the region of interest), which need to be specified in `download_modis_https` and `download_oco2_https` (from `er3t/util`). For example, for APP1 and APP2, the only user inputs are the date and time and the region of interest – in this case September 2, 2019, with the westernmost, easternmost, southernmost, and northernmost longitudes and latitudes of 109°W, 107°W, 37°N, and 39°N. In order for EaR^{3}T to access any data archives such as NASA Earthdata, the user needs to create an account with them and store the credentials locally (detailed instructions are provided separately along with the EaR^{3}T distribution).

After the data acquisition step, the satellite data are fed into the pre-processing step for 1) atmospheric gases (`er3t/pre/atm`), 2) clouds (`er3t/pre/cld`), 3) surface (`er3t/pre/sfc`) as shown in Figure 1. In the default configuration of the APP1, the standard US atmosphere (Anderson et al., 1986; included in the EaR^{3}T repository) is used within `atm`. EaR^{3}T supports the input of user-specified atmospheric profiles, e.g., atmospheric profiles from reanalysis data for APP2 as described in Schmidt et al. (2022), by making changes in `atm_atmmod` (from `er3t/pre/atm`). Subsequently, molecular scattering coefficients are calculated by `cal_mol_ext` (from `er3t/util`), and absorption coefficients for atmospheric gases are generated by (`er3t/pre/abs`). At the current development stage, two options are available:

1. Line-by-line (used by APP1): The repository includes a sample file of absorption coefficient profiles for a subset of wavelengths within OCO-2's Oxygen A-Band channel, corresponding to a range of atmospheric transmittance values from low (opaque) to high (so-called "continuum" wavelength). They were generated by an external code (Schmidt et al., 2022) based on OCO-2's line-by-line absorption coefficient database (ABSCO, Payne et al.,

https://doi.org/10.5194/amt-2022-143
Preprint. Discussion started: 29 June 2022

2020). For each wavelength, there are hundreds of individual absorption coefficient profiles, spectrally spaced at the native resolution of ABSCO, and ranging across the instrument line shape (ILS, also known as the slit function) of the OCO-2 Oxygen A-Band spectrometer. The ILS, as well as the incident solar irradiance, are also included in the file. In subsequent steps, EaR^{3}T performs RT calculations at the native spectral resolution of ABSCO, but then combines the output by convolving with the ILS and outputs OCO-2 radiances or reflectances at the subset of wavelengths. For probabilistic (Monte Carlo) RT solvers such as MCARaTS, the number of photons can be kept relatively low (e.g., 10^6 photons), and can be adjusted according to the values of the ILS at a particular ABSCO wavelength. Any uncertainty at the ABSCO spectral resolution due to photon noise is greatly reduced by convolving with the ILS for the final output.

2. Correlated-k (used by APP2): This approach (Mlawer et al., 1997) is appropriate for instruments such as MODIS with much coarser spectral resolution than OCO-2, as well as for broadband calculations. In contrast to the line-by-line approach, RT calculations are not performed at the native resolution of the absorption database, but at Gaussian quadrature points (called “g’s”) that represent the full range of sorted absorption coefficients, and then combined using Gaussian quadrature weights. The repository includes an absorption database from Coddington et al. (2008), developed specifically for a radiometer with moderate spectral resolution on the basis of HITRAN (high-resolution transmission molecular absorption database) 2004 (Rothman et al., 2005). It was created for the ILS of the airborne Solar Spectral Flux Radiometer (SSFR, Pilewskie et al., 2003), but is applied to MODIS here, which has a moderate spectral resolution of 8-12 nm with 20-50 nm bandwidths. It uses 16 absorption coefficient bins (g’s) per target wavelength, which are calculated by EaR^{3}T with the Coddington et al. (2008) database using the mixing ratios of atmospheric gases in the previously ingested profile. In future implementations, the code will be updated to enable flexible ILS and broadband calculations.

The `er3t/pre/cld` module calculates extinction, thermodynamic phase, and effective droplet radius of clouds from the input data. The `er3t/pre/pha` module creates the required single scattering albedo and scattering phase function. The default is a Henyey-Greenstein phase function with a fixed asymmetry parameter of 0.85. It is, however, recommended to also install libRadtran to enable the usage of Mie phase functions based on thermodynamic phase, effective

https://doi.org/10.5194/amt-2022-143
Preprint. Discussion started: 29 June 2022

droplet radius, and wavelength. In this study, APP1 and APP2 use Mie phase functions calculated from Legendre polynomial coefficients distributed along with libRadtran based on the wavelength and cloud droplet effective radius. In the future, EaR^{3}T will include stand-alone phase functions, which can be chosen on the basis of droplet size distributions in addition to effective radius. It is also possible to include aerosols in a similar fashion as clouds. This is done with the `er3t/pre/aer` module. In the case of aerosols, spectral single scattering albedo and asymmetry parameter are required as inputs in addition to the extinction fields.

After the optical properties are calculated, they are passed into the 3D-RT step (`er3t/rtm/mca`). In addition to MCARaTS, planned solvers for the future include MYSTIC (Monte Carlo code for the physically correct tracing of photons in cloudy atmospheres, Mayer, 2009) and SHDOM (Spherical Harmonic Discrete Ordinate Method, Evans, 1998; Pincus and Evans, 2009). This step performs the setup of RT solver-specified input parameters and data files, distributing runs over multiple CPUs, and post-processing RT output files into a single, user-friendly HDF5 file. For example, when radiance is specified as output (default in APP1 and APP2), key information such as the radiance field and its standard deviation are stored in the final HDF5 file (details see Table 1). The EaR^{3}T documentation only provides detailed instructions of installing the RT solvers (currently only MCARaTS) and libRadtran.

While the EaR^{3}T repository comes with various applications such as APP1 and APP2, described above, the functions used by these master or 'wrapper' programs can be organized in different ways, where the existing applications serve as templates for a quick start when developing new applications. The functions used by the master code pass information through the various steps as Python objects. For example, in `examples/01_oco2_rad-sim.py`, the downloaded and processed satellite data are stored into the `sat` object. Later, the `sat` object is passed into an EaR^{3}T function to create the `cld` object that contains cloud optical properties. Similarly, EaR^{3}T provides functions to create the `atm`, and `sfc` objects with optical properties for atmospheric gases and the surface. These objects (`atm`, `cld`, `sfc`) are in turn passed on to solver-specific modules for performing RT calculations. The user can choose to save the data of the intermediate objects into Python pickle files after the first run. In this way, multiple calls with identical input can re-use existing data, which accelerates the processing time of EaR^{3}T. Unless the user specifies the `overwrite` keyword argument in the object call to reject saving pickle files, these shortcuts save significant time. Moreover, EaR^{3}T is capable of distributing simulations over multiple CPUs

https://doi.org/10.5194/amt-2022-143
Preprint. Discussion started: 29 June 2022

Atmospheric Measurement Techniques Discussions

to accelerate the calculations, which is useful for potential future application of later EaR^{3}T or EaR^{3}T-like codes in operational or large-scale data processing.

In the following sections, we discuss results obtained from EaR^{3}T, starting with those from `examples/01_oco2_rad-sim.py` and `examples/02_modis_rad-sim.py` (section 4), `examples/03_spns_flux-sim.py` (section 5), and concluding with `examples/04_cam_nadir_rad-sim.py` (section 6). The detailed RT setup for the four applications is provided in Table 2.

	APP1 - Radiance for MODIS	APP2 - Radiance for OCO-2	APP3 - Irradiance for SPN-S	APP4 - Radiance for CNN/ASC
Wavelength	760 nm	650 nm	745 nm	600 nm
Atmospheric profile	US Standard Atmosphere	Reanalysis	AFGL - Tropical Summer	AFGL - Tropical Summer
Solar zenith and azimuth angles	Acquired from OCO-2 data	Acquired from MODIS data	Calculated from aircraft navigational data	Calculated from aircraft navigational data
Surface albedo	Scaled from MYD09A1	Acquired from MYD09A1	0.03	0.03
Sensor zenith and azimuth angles	Acquired from OCO-2 data	Acquired from MODIS data	Zenith	Nadir
Cloud Optical Thickness	Retrieved from MODIS reflectance through IPA method	Retrieved from MODIS reflectance through IPA method	Acquired from AHI L2 Cloud Product	Retrieved through 1) IPA method, 2) CNN model
Cloud effective radius	Acquired from MYD06L2	Acquired from MYD06L2	N/A	N/A

Phase function	Mie	Mie	Henyey-Greenstein (g=0.85)	Henyey-Greenstein (g=0.85)
Cloud location	CTH from MYD06L2 minus 1 km to CTH	CTH from MYD06L2 minus 1 km to CTH	2 km to 3 km	1 km to 2 km
Number of Photons	1×10^{8}	1×10^{8}	1×10^{7}	1×10^{8}

Table 2: RT parameters for APP1, APP2, APP3, and APP4.

4. EaR^{3}T as a 3D Satellite Radiance Simulator

This section demonstrates the automated 3D radiance simulation for satellite instruments by EaR^{3}T for OCO-2 and MODIS measured radiance based on publicly available MODIS retrieval products. The OCO-2 application is an example of radiance consistency between two distinct satellite instruments where the measurements of one (here, OCO-2) are compared with the simulations based on data products from the other (here, MODIS). The MODIS application, on the other hand, is an example of radiance self-consistency. We will show how inconsistencies can be used for detecting cloud and surface property retrieval biases.

4.1 OCO-2 (APP1)

The OCO-2 radiance measurements at 768.52 nm for our sample scene in the context of MODIS imagery were shown in Figure 2. For that track segment, Figure 5 shows the simulated radiance along with the measurements as a function of latitude. The radiance was averaged over every 0.01° latitude window from 37° N to 39° N (the standard deviation within the bin indicated by the shaded color). In clear-sky regions (e.g., around 38.2º N), the simulations (red) are systematically higher than the measurements (black), even though the footprint-level OCO-2 retrieval was used to scale the MYD09 field as described in section 2.2.2 (Figure 4). This is because, unlike the MYD09 algorithm which relies on multiple overpasses and multiple-days for cloud-clearing, the OCO-2 retrieval is done for any clear footprint. Clouds in the vicinity lead to enhanced diffuse illumination that is erroneously attributed to the surface reflectance itself. The EaR^{3}T IPA calculations of the clear-sky pixels (blue) essentially reverse the 3D effect and therefore match the observations better. The 3D calculations enhance the reflectance through the very same 3D cloud

https://doi.org/10.5194/amt-2022-143
Preprint. Discussion started: 29 June 2022

effects that led to the enhanced surface illumination in the first place. It is possible to correct this effect by down-scaling the surface reflectance according to the ratio between clear-sky 3D and IPA calculations, but this process is currently not automated.

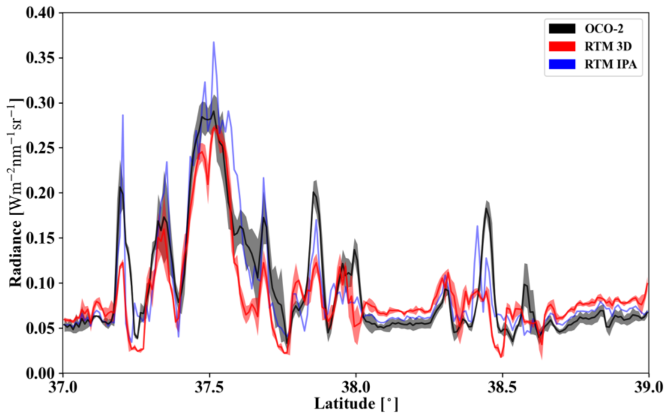

Figure 5. Latitudinally averaged (0.01° spacing) radiance calculations from EaR^{3}T (red: 3D, blue: IPA) and OCO-2 measured radiance at 768.52 nm (black). The solar zenith angle for the radiance simulation case is 33.75°.

In the cloudy locations, the IPA calculations match the OCO-2 observations on a footprint-by-footprint level, demonstrating that wind and parallax corrections were performed successfully. Of course, there is not always a perfect agreement because of morphological changes in the cloud field over the course of six minutes. It is, however, apparent that the 3D calculations agree to a much lesser extent with the observations than the IPA calculations. Just like the mismatch for the clear-sky pixels indicates a bias in the input surface reflectance, the bias here means that the input cloud properties (most importantly COT) are inaccurate. For most of the reflectance peaks, the 3D simulations are too low, which means that the input COT is biased low. This is due to 3D cloud effects on the MODIS-based cloud retrieval. Since they are done with IPA, any net horizontal photon transport is not considered, which leads to an apparent surface brightening as noted above, at the expense of the cloud brightness. As a result, the COT from darker clouds is significantly underestimated. This commonly known problem, with several aspects discussed in the subsequent EaR^{3}T applications, can be identified by radiance consistency checks such as the one shown in Figure 5, and mitigated by novel types of cloud retrievals that do take horizontal photon transport into account (section 6).

https://doi.org/10.5194/amt-2022-143
Preprint. Discussion started: 29 June 2022

4.2 MODIS (APP2)

To go beyond the OCO-2 track and understand the bias between simulated and observed radiances from a domain perspective, we now consider the radiance simulations for the MODIS 650 nm channel. The setup is exactly the same as for the OCO-2 simulations, except that 1) the viewing zenith angle is set to the average viewing zenith angle of MODIS within the shown domain (instead of OCO-2), and 2) the surface reflectances from MYD09 are used directly, this time from the 650 nm channel without rescaling. Figure 6a shows the MODIS measured radiance field, while Figure 6b shows the EaR^{3}T 3D simulations. Visually, the clouds from the EaR^{3}T simulation are generally darker than the observed clouds, which is in line with our aforementioned explanation of net horizontal photon transport. They are also blurrier because radiative smoothing (Marshak et al., 1995) propagates into the retrieved COT fields, which are subsequently used as input to EaR^{3}T. To look at darkening and smoothing effects more quantitatively, Figure 7 shows a heatmap plot of simulated radiance versus observed radiance. It shows that the radiance for cloud-covered pixels (labeled "cloudy") from EaR^{3}T are mostly low-biased while good agreement between simulations and observations was achieved for clear-sky radiance (labeled "clear-sky"). The good agreement over clear-sky regions is expected. As mentioned above, we use MYD09 as surface reflectance input, which in contrast to the OCO-2 surface reflectance product is appropriately cloud-screened and therefore does not have a reflectance high bias. There is, of course, a reflectance enhancement in the vicinity of clouds, but that is captured by the EaR^{3}T calculations. The fact that the calculations agree with the observations even for clear-sky pixels in the vicinity of clouds, shows that the concept of radiance consistency works to ensure correct satellite retrievals even in presence of clouds. It also corroborates our observation from section 4.1 that COT_{IPA} is low biased. Since the MODIS reflectance is *not* self-consistent with respect to COT_{IPA} as shown for the *cloudy* pixels in Figure 7, we can identify a bias in the cloud properties even without knowing the ground truth of COT. On the other hand, successful closure in radiance (self-consistency) would provide an indication that the input fields including COT are accurate, although it is certainly a weaker metric than direct verification of the retrievals through aircraft satellite retrieval validation with in-situ instruments.

https://doi.org/10.5194/amt-2022-143
Preprint. Discussion started: 29 June 2022

Atmospheric Measurement Techniques
Discussions

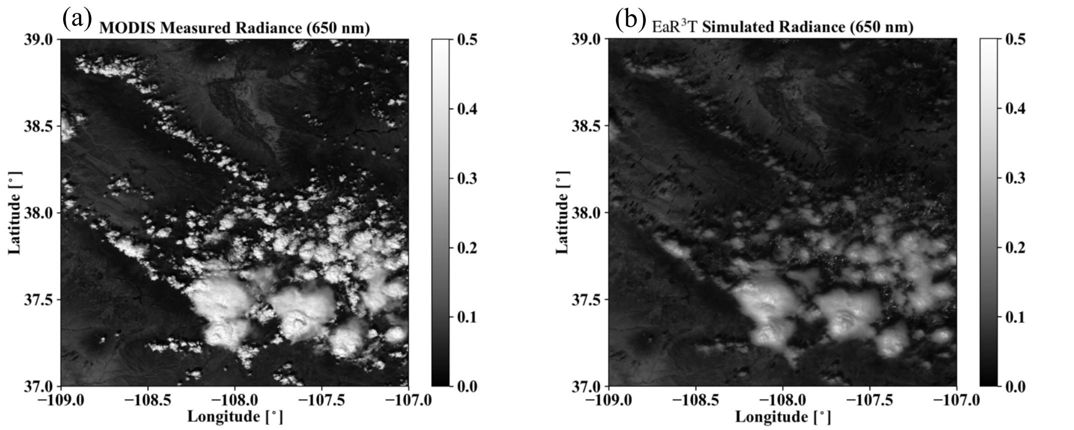

Figure 6. **(a)** MODIS measured radiance in channel 1 (650 nm). **(b)** Simulated 3D radiance at 650 nm from EaR^{3}T. The solar zenith angle for the radiance simulation case is 34.42°.

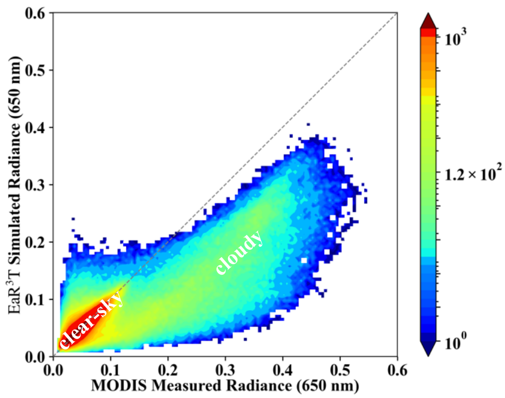

Figure 7. Heatmap plot of EaR^{3}T simulated 3D radiance vs. MODIS measured radiance at 650 nm.

Summarizing the two satellite radiance simulator applications, one can say that EaR^{3}T enables a radiance consistency check for inhomogeneous scenes. We demonstrated that a lack of simulation-observation consistency (MODIS versus OCO-2) and self-consistency (MODIS versus MODIS) can be traced back to biased surface reflectance or cloud fields in the simulator input. This can become a diagnostic tool for the quality of retrieval products from future or current missions, even when the ground truth is not known.

For technical reference: The MODIS simulation took about one hour on a Linux workstation with 12 CPUs for three 3D RT runs with 10^8 photons each. With a slightly modified setup and parallelization, the automation can be easily applied for entire satellite orbits, although more research is required to optimize the computation speed depending on the desired output accuracy.

5. EaR^{3}T as 3D Aircraft Irradiance Simulator (APP3)

In contrast to the previous applications that focused on satellite remote sensing, we will now be applying EaR^{3}T to quantify 3D cloud retrieval biases through direct, systematic validation of imagery-derived *irradiances* against aircraft measurements, instead of using the indirect path of radiance consistency in section 4. Previous studies (e.g., Schmidt et al., 2007; Kindel et al., 2010) conducted radiative closure between remote sensing derived and measured irradiance using isolated flight legs as case studies. Here, with the efficiency afforded by the automated nature of EaR^{3}T, we are able to conduct radiative closure of irradiance through a statistical approach that employs campaign-scale amounts of measurement data. Specifically, we used EaR^{3}T to perform large-scale downwelling irradiance simulations at 745 nm based on geostationary cloud retrievals from AHI for the CAMP^{2}Ex campaign, and directly compare these simulations to the SPN-S measured irradiances onboard the P-3 aircraft. This is done for all below-cloud legs from the entire campaign with the aim to assess the degree to which satellite-derived near-surface irradiances reproduce the true conditions below clouds.

The irradiance simulation process is similar to the previously described radiance simulation in section 4, with only a few modifications. First, we used cloud optical properties from the AHI cloud product (COT, CER and CTH) as direct inputs into EaR^{3}T. Secondly, we used a constant ocean surface reflectance value of 0.03. Such simplification in surface albedo is made under the assumption that 1) the ocean surface is calm with no whitecaps, and that 2) the Lambertian bidirectional reflectance distribution function (BRDF) is sufficient (instead of directionally dependent BRDF) to represent surface albedo for the irradiance calculation. Since the ocean surface albedo can greatly differ from 0.03 when the Sun is extremely low (Li et al., 2006), we excluded data under low-Sun conditions where the SZA is greater than 45°. Lastly, since EaR^{3}T can only perform 3D simulations for a domain at a single specified solar geometry, we divided each CAMP^{2}Ex research flight into small flight track segments where each segment contains 6

Atmospheric Measurement Techniques Discussions

minutes of flight time. The size and shape of the flight track segments can vary significantly due to the aircraft maneuvers, aircraft direction, aircraft speed, etc. For each flight track segment, EaR^{3}T performs irradiance simulations for a domain that extends half a degree at an averaged solar zenith angle. In contrast to the radiance simulation output, which is two-dimensional at a specified altitude and sensor geometry, the irradiance simulation output is three dimensional. In addition to x (longitude) and y (latitude) vectors, it has a vertical dimension along z (altitude). From the simulated three-dimensional irradiance field, the irradiance for the flight track segment is interpolated to the x-y-z location (longitude, latitude, and altitude) of the aircraft. EaR^{3}T automatically sub-divides the flight track into tiles encompassing track segments, and extracts the necessary information from the aircraft navigational data. Based on the aircraft time and position, EaR^{3}T downloads the AHI cloud product that is closest in time and space to the domain containing the flight track segment.

Figure 8 shows simulated irradiance for a sample flight track below clouds on 20 September, 2019. Figure 8a shows the flight track overlaid on AHI imagery. Figure 8b shows 3D (in red) and IPA (in blue) downwelling irradiance simulations for the highlighted flight track in Figure 8a, as well as measurements by the SPN-S (in black). Since the 3D and IPA simulations are performed separately at discrete solar and sensor geometries for each flight track segment based on potentially changing cloud fields from one geostationary satellite image to the next, discontinuities in the calculations (indicated by gray dashed lines) are expected. The diffuse irradiance (downwelling and upwelling) can also be simulated and compared with radiometer measurements (not shown here). Since the irradiance was simulated/measured below clouds, high values of downwelling irradiance indicate thin-cloud or cloud-free regions while low values of downwelling irradiance indicate thick-cloud regions. The simulations successfully captured this general behavior – clouds thickened from west to east until around 121.25° E, and thinned eastwards. However, the fine-scale variabilities in irradiance were not captured by the simulations due to the coarse resolution of COT in the AHI cloud product (3-5 km). Additionally, the simulations also missed the clear-sky regions in the very east and west of the flight track as indicated by high downwelling irradiance values measured by SPN-S. This is probably also due to the coarse resolution of the AHI COT product where small cloud gaps are not represented. Large discrepancies between simulations and observations occur in the mid-section of the flight track where clouds are present (e.g., longitude range from 121.15° to 121.3°). Although the 3D

https://doi.org/10.5194/amt-2022-143
Preprint. Discussion started: 29 June 2022

Atmospheric Measurement Techniques Discussions

calculations differ somewhat from the IPA results, they are both biased high, likely because the input COT (the IPA-retrieved AHI product) is biased low. This bias is caused by the same mechanism that was discussed earlier in the examples from MODIS (section 4.2). This begs the question whether this is true for the entire field mission. To answer the question, we performed a *systematic* comparison of the cloud transmittance for *all* available below-cloud flight tracks from CAMP^{2}Ex, using EaR^{3}T's automated processing pipeline.

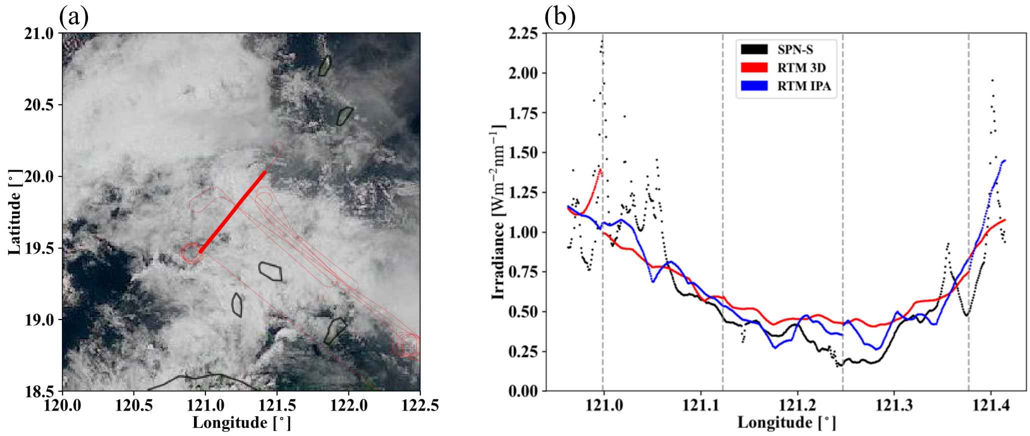

Figure 8. **(a)** Flight track overlay HIMAWARI AHI RGB imagery over the Philippine Sea on 20 September, 2019. **(b)** Measured downwelling irradiance from SPN-S at 745 nm and calculated 3D and IPA irradiance from EaR^{3}T for the highlighted flight track in (a).

For this comparison, we use transmittance instead of irradiance because it has less diurnal dependence. The transmittance is calculated by dividing the downwelling irradiance below clouds by the downwelling irradiance at the top of the atmosphere extracted from the Kurucz solar spectra (Kurucz, 1992). Figure 9 shows the histograms of the simulated and measured cloud transmittance from all below-cloud legs. The average values are indicated by dashed lines. Although the averaged values of IPA and 3D transmittance are close, their distributions are completely different. Only the 3D calculations and the measured transmittance reach values beyond 1. This occurs in clear-sky regions in the vicinity of clouds that receive photons scattered by the clouds as previously discussed for the OCO-2 application.

https://doi.org/10.5194/amt-2022-143
Preprint. Discussion started: 29 June 2022

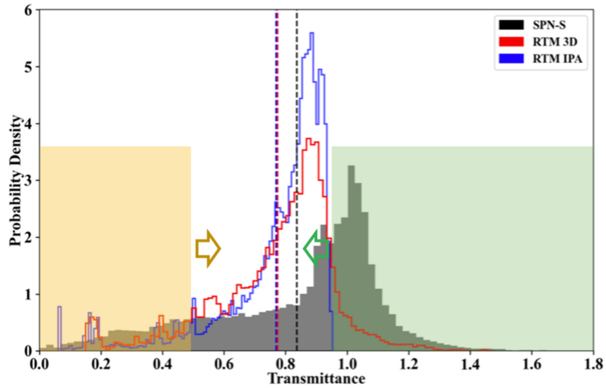

Figure 9. Histogram of measured transmittance from SPN-S at 745 nm (black) and calculated 3D (red) and IPA (blue) transmittance from EaR^{3}T for all the below-cloud flight tracks during CAMP^{2}Ex in 2019. The mean values are indicated by dashed lines. The yellow shaded area represents the relatively low transmittance region where the probability density of the observed transmittance (black) is greater than the calculations. Vice versa for the green shaded area.

Both the distribution and the mean value of the simulations are different from the observations – the simulation histogram peaks at around 0.9 while the observation histogram peaks at around 1. The histograms indicate that the RT simulations miss most of the clear-sky conditions because of the coarse resolution of the AHI cloud product. If clouds underfill a pixel, AHI interprets the pixel as cloudy in most cases. This leads to an underestimation of clear-sky regions since cumulus and high cirrus were ubiquitous during CAMP^{2}Ex. The area on the left (highlighted in yellow) has low cloud transmittance associated with thick clouds. In this range, the histograms of the calculations are generally below the observations, and the PDF of the calculations is offset to the right (indicated by the yellow arrow). This means that the transmittance is overestimated by both IPA and 3D RT, and thus that the COT of thick clouds is underestimated, consistent with what we found before (Figure 8b). The high-transmittance end (highlighted in green) is associated with clear-sky and thin clouds. Here, the peak of the PDF is shifted to the left (green arrow), and the calculations are biased low. This is caused by a combination of 1) the overestimation in COT of thin clouds due a 3D bias in the AHI IPA retrieval, 2) the aforementioned resolution effect that underestimates the occurrence of clear-sky regions, and 3) net horizontal photon transport from clouds into clear-sky pixels. Overall, the low bias dominates, as is apparent from mean values of

https://doi.org/10.5194/amt-2022-143
Preprint. Discussion started: 29 June 2022

the distributions. There is an overall low bias of 10%, and the combined imager resolution and 3D effects do not compensate each other.

Summarizing, this application demonstrates that EaR^3T's automation feature allows systematic simulation-to-observation comparisons. If aircraft observations are available, then closure between satellite-derived irradiance and suborbital measurements is a more powerful verification of satellite cloud retrieval products than the radiance consistency from the earlier stand-alone satellite applications. Even more powerful is the new approach to process the data from an entire field mission for assessing the quality of cloud products in a region of interest (in this case, the $CAMP^2Ex$ area of operation). We found that the bias between observed and satellite-derived cloud transmittance is partially caused by the coarse imager resolution, and partially by 3D effects, although other retrieval artifacts could also play a role. Although important for future research, it is beyond the scope of this paper to disentangle these effects.

6. EaR^3T for Mitigating 3D Cloud Retrieval Biases (APP4)

In this section, we will use a high-resolution imagery from a radiometrically calibrated all-sky camera flown during the $CAMP^2Ex$ to isolate the 3D bias (sometimes referred to as IPA bias) and explore its mitigation with a newly developed CNN cloud retrieval framework (Nataraja et al., 2022). The CNN, unlike IPA, takes pixel-to-pixel net horizontal photon transport into account. It exploits the spatial context of pixels in cloud radiance imagery, and extracts a higher-dimensional, multi-scale representation of the radiance to retrieve COT fields as the output. It does so by learning on "training data", which in this case was input radiance and COT pairs synthetically generated by EaR^3T using LES data from the Sulu Sea. The best CNN model, trained on different coarsened resolutions of the data pairs, is included within the EaR^3T repository. For APP4, this CNN is applied to real imagery data for the first time, which in our case are near-nadir observations by the all-sky camera (section 2.2.5) that flew in $CAMP^2Ex$.

The CNN model was trained at a single (fixed) sun-sensor geometry (solar zenith angle, SZA=29.2°; solar azimuth angle, SAA=323.8°, viewing zenith angle, VZA=0º), at a spatial resolution of 100 m. We therefore chose a camera scene with a matching SZA (28.9°), and rotated the radiance imagery to match SAA=323.8°, and subsequently gridded the 8-12 m native resolution camera data to 100 m. Figure 10a shows the RGB imagery captured by the all-sky camera over the Philippine Sea at 02:10:06 UTC on 5 October 2019. The Sun is located at the

https://doi.org/10.5194/amt-2022-143
Preprint. Discussion started: 29 June 2022

Atmospheric Measurement Techniques Discussions
Open Access
EGU

southeast and can be easily identified from the sun glint. Note that this image has not yet been geolocated; it is depicted as acquired in the aircraft reference frame. Figure 10b shows the rotated scene of the red channel radiance for the region encircled in yellow in Figure 10a. The sun (as indicated by the yellow arrow) is now at SAA=323.8°. Inside a 6.4x6.4 km^2 core area, the 100 m gridded radiance field is shown instead of the native-resolution imagery.

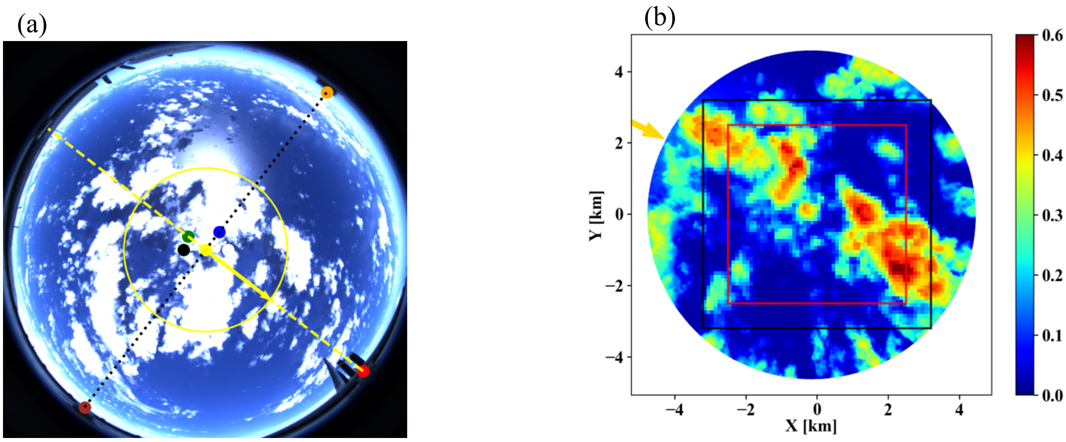

Figure 10. **(a)** RGB imagery of nadir-viewing all-sky camera deployed during CAMP^{2}Ex for a cloud scene centered at [123.392°E, 15.2744°N] over the Philippine Sea at 02:10:06 UTC on 5 October, 2019. The lines indicate the axis of the aircraft (yellow) and wing to wing (across, black). The yellow circle shows the approximate field of view that is geolocated for (b); the dots denote various directions from the nadir point. **(b)** Gridded radiance for the square area indicated by solid black lines in (a) with a pixel size of 64x64 and spatial resolution of 100 m. Later for the comparison of COT and RT calculations, only the data from the red square box (50x50) is used. The solar position (azimuth) is indicated by the yellow arrow.

From the radiance field, we used both the traditional IPA (based on the two-stream approximation) and the new CNN to retrieve COT fields. Figure 11 shows the COT_{IPA} and COT_{CNN} fields, which are visually quite different. For relatively thick clouds (e.g., at (x=2, y=22)), the CNN tends to retrieve larger COT values than COT_{IPA}. Also, it returns more spatial structure than the IPA (e.g., around {2,-1}). To assess how either retrieval performs, we now apply the radiance self-consistency approach introduced with MODIS data in section 4.2. Using both the IPA and the CNN retrieval as input, we had EaR^{3}T calculate the (synthetic) radiance that the camera should have observed if the retrieval were accurate. The clouds are assumed to be located at 1-2 km. Such

https://doi.org/10.5194/amt-2022-143
Preprint. Discussion started: 29 June 2022

an assumption is inferred from low-level aircraft observations of clouds on the same day. These radiance fields are shown in Figure 12, and can be compared to the red box from Figure 10b, which marks a region where 12 edge pixels have been removed from the original domain. This was necessary because the CNN performs poorly at edge pixels, and because the 3D calculations use periodic boundary conditions.

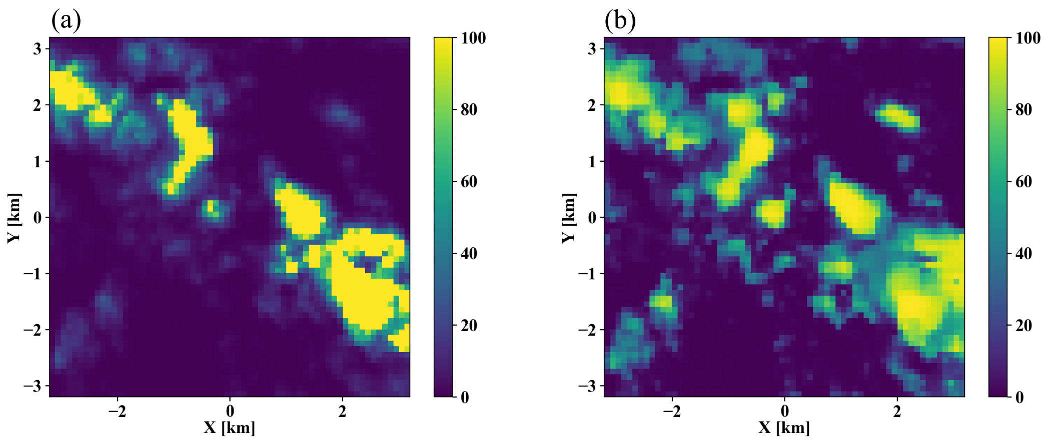

Figure 11. Cloud optical thickness for the gridded radiance in Figure 10b **(a)** estimated by IPA and **(b)** predicted by CNN.

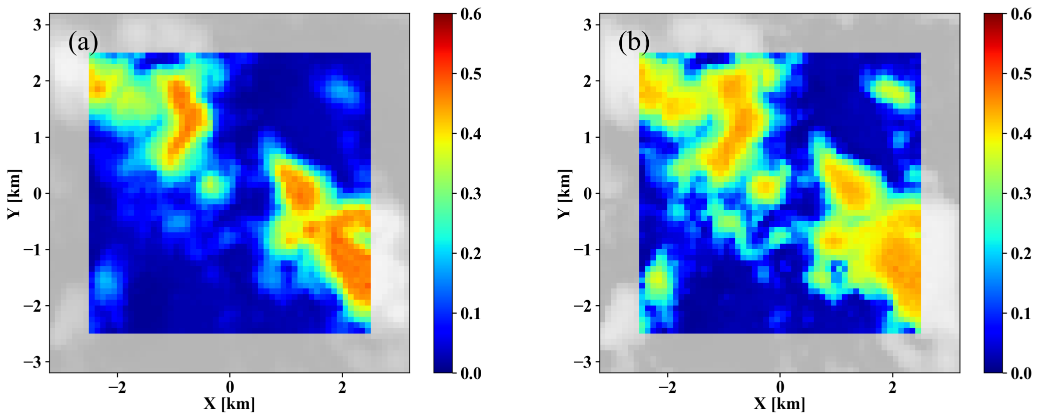

Figure 12. 3D radiance calculations from EaR^{3}T at 600 nm based on cloud optical thickness field **(a)** estimated by Two-Stream approximation and **(b)** predicted by the CNN. The calculations were originally performed

https://doi.org/10.5194/amt-2022-143
Preprint. Discussion started: 29 June 2022

for the 64x64 domain. Then 7 pixels along each side of the domain (contoured in gray) were excluded, which resulted in a 50x50 domain.

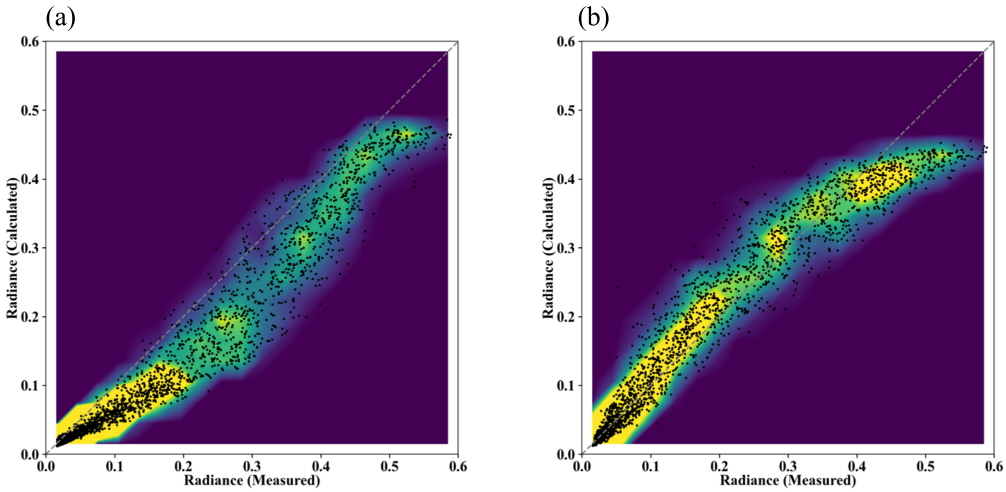

Figure 13. Scatter plot overlays 2D histogram of 3D radiance calculations at 600 nm based on cloud optical thickness **(a)** estimated by Two-Stream approximation and **(b)** predicted by the CNN vs. measured red channel radiance from all-sky camera.

As evident from the brightest pixels in Figures 12b and 10b, the radiances simulated on the basis of the CNN COT input are markedly lower than actually observed by the camera. This is because the CNN was trained on a LES dataset with limited COT range that excluded the largest COT that occurred in practice. This means that the observational data went beyond the original training envelope of the CNN, which highlights the importance of choosing the CNN training data carefully for a given region. In Figure 13, the simulations are directly compared with the original observations, confirming that indeed the CNN-generated data are below the observations on the high radiance end. Otherwise, the CNN-generated radiances agree with the observations. By contrast, the IPA-generated data are systematically lower than the observations, over the dynamic range of the COT, which is indicative of the 3D retrieval bias that we discussed earlier. Here again, the self-consistency approach proves useful despite the absence of ground truth data for the COT. This is extremely helpful because in reality satellite remote sensing does not have the ground truth of COT, whereas radiance measurements are always available. For the CNN, the self-consistency

https://doi.org/10.5194/amt-2022-143
Preprint. Discussion started: 29 June 2022

Atmospheric Measurement Techniques
Discussions

of the radiance is remarkable for the thinner clouds (radiance smaller than 0.4), which encompass 83.5% of the total number of image pixels.

Finally, we use EaR^{3}T to propagate the 3D cloud retrieval bias into the associated bias in estimating the cloud radiative effect from passive imagery retrievals, which means that we are returning from a remote sensing to an energy perspective (irradiance) at the end of the paper. The calculated cloud radiative effects (CRE) of both below-clouds (at the surface) and above-clouds (at 3 km) are shown in Figure 14a and 14b. The most important histograms are those from 3D irradiance calculations based on the CNN retrievals (black solid line), as this combination would be used in a next-generation framework for deriving CRE from passive remote sensing, and the other would be IPA irradiance calculations based on the IPA retrieval (red solid line), as done in the traditional (heritage) approach. The dashed lines are the other combinations. The mean values (red vs. black) indicate that in our case the traditional approach would lead to a high bias of more than to 25% both at the surface and above clouds. Here again, 3D biases do not cancel each other out in the domain average. If the CNN had better fidelity even for optically thick clouds, the real bias in CRE would be even larger. A minor, but interesting finding is that regardless of which COT retrieval is used, the mean CRE is very similar for IPA and 3D irradiance calculations, even though the PDFs are very dissimilar. By far the largest impact on accuracy comes from the retrieval technique, not from the subsequent CRE calculations. Here again, the self-consistency check turns out as a powerful metric to assess retrieval accuracy. Of course, we only used a single case in this part of the paper. For future evaluation of the CNN versus the IPA, one would need to process larger quantities of data in an automated fashion as done in the first part of the paper. This is beyond the scope of this introductory paper, and will be included in future releases of EaR^{3}T and the CNN.

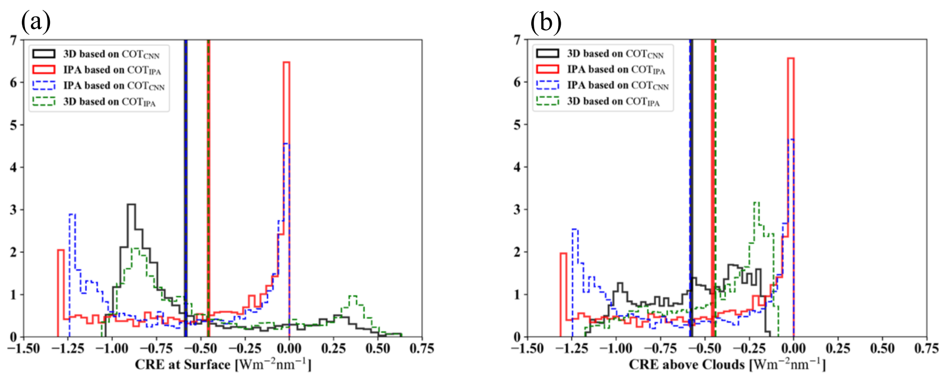

https://doi.org/10.5194/amt-2022-143
Preprint. Discussion started: 29 June 2022

Atmospheric Measurement Techniques Discussions

Figure 14. Histograms of cloud radiative effects derived from 1) 3D irradiance calculations based on COT_{CNN} (solid black), 2) IPA irradiance calculations based on COT_{IPA} (solid red), 3) IPA irradiance calculations based on COT_{CNN} (dashed blue), and 4) 3D irradiance calculations based on COT_{IPA} (dashed green) both **(a)** at the surface and **(b)** above the clouds. The mean values are indicated by vertical lines.

7. Summary and Conclusion

In this paper, we introduced EaR^{3}T, a toolbox that provides high-level interfaces to automate and facilitate 1D- and 3D-RT calculations. We presented applications that used EaR^{3}T to:

a) build a processing pipeline that can automatically simulate 3D radiance fields for satellite instruments (currently OCO-2 and MODIS) from publicly available satellite surface and cloud products at any given time over any specific region;
b) build a processing pipeline that can automatically simulate irradiance along all flight legs of aircraft missions, based on geostationary cloud products;
c) simulate radiance and irradiance for high-resolution COT fields retrieved from an airborne camera, using both a traditional 1D-RT (IPA) approach, and a newly developed 3D-RT (CNN) approach that considers the spatial context of a pixel.

Unlike other satellite simulators that employ 1D-RT, EaR^{3}T is capable of performing the radiance and irradiance calculations in 3D-RT mode. Optionally, it can be turned off to link back to traditional 1D-RT codes, and to calculate 3D perturbations by considering the changes of 3D-RT fields relative to the 1D-RT baseline.

With the processing pipeline under a) (APP1 and APP2, section 4), we prototyped a 3D-RT powered radiance loop that is envisioned for upcoming satellite missions such as EarthCARE and AOS. Retrieved cloud fields (in our case, from MODIS and from an airborne camera) are fed back into a 3D-RT simulation engine to calculate at-sensor radiances, which are then compared with the original measurements. Beyond currently included sensors, others can be added easily, taking advantage of the modular design of EaR^{3}T. This radiance closure loop facilitates the evaluation of passive imagery products, especially under spatially inhomogeneous cloud conditions. The automation of EaR^{3}T permits calculations at any time and over any given region, and statistics can be built by looping over entire orbits as necessary. The concept of radiance consistency could be valuable even for existing imagery datasets because it allows the automated quantification of 3D-RT biases even without ground truth such as airborne irradiance from

https://doi.org/10.5194/amt-2022-143
Preprint. Discussion started: 29 June 2022

Atmospheric Measurement Techniques Discussions

suborbital activities. In the future it should be possible to include a 3D-RT pipeline such as EaR^{3}T into operational processing of satellite derived data products.

Benefitting from the automation of EaR^{3}T in b) (APP3, section 5), we performed 3D-RT irradiance calculations for the entire CAMP^{2}Ex field campaign, moving well beyond radiation closure case studies, and instead systematically evaluating satellite-derived radiation fields with aircraft data for an entire region. From the comparison based on all below-cloud flight tracks during the entire campaign, we found that the satellite-derived cloud transmittance was biased low by 10% compared to the observations when relying on the heritage satellite cloud product.

From the statistical results of the CAMP^{2}Ex irradiance closure in b), we concluded that the bias between satellite-derived irradiances and the ground truth from aircraft measurements was either due to the coarse spatial resolution of the geostationary imagery products, or caused by 3D-RT effects. To minimize the coarse-resolution part of the bias and thus to isolate the 3D-RT bias, we used high-resolution airborne camera imagery in c) (APP4, section 6), and found that even with increased imager resolution, biases persisted. The at-sensor radiance derived from IPA COT retrievals was inconsistent with the original measurements. For cloudy pixels, the calculated radiance was well below the observations, confirming an overall low bias in IPA COT. This low bias could be largely mitigated with the context-aware CNN developed separately in Nataraja et al. (2022) and included in EaR^{3}T. Of course, this novel technique has limitations. For example, the camera reflectance data went beyond the CNN training envelope, which would need to be extended to larger COT in the future. In addition, the CNN only reproduces two-dimensional clouds fields and does not provide access to the vertical dimension, which will be the next frontier to tackle. Still, the greatly improved radiance consistency from COT_{IPA} to COT_{CNN} indicates that the EaR^{3}T-LES-CNN approach shows great promise for the mitigation of 3D-RT biases associated with heritage cloud retrievals. We also discovered that for this particular case, the CRE calculated from traditional 1D cloud products can introduce a warming bias of at least 25% at the surface and above clouds.

EaR^{3}T has proven to be capable of facilitating 3D-RT calculations for both remote sensing and radiative energy studies. Beyond the applications described in this paper, EaR^{3}T has already been extensively used by a series of on-going research projects such as producing massive 3D-RT calculations as training data for a new generation of CNN models (Nataraja et al., 2022), evaluating 3D cloud radiative effects associated with aerosols (Gristey et al., 2022), creating flight track and

https://doi.org/10.5194/amt-2022-143
Preprint. Discussion started: 29 June 2022

Atmospheric Measurement Techniques Discussions
Open Access

satellite track simulations for mission planning etc. More development effort will be invested into EaR^{3}T in the future, with the goals of minimizing the barriers to using 3D-RT calculations, and to promote 3D cloud studies. EaR^{3}T will continue to be an educational tool driven by graduate students. From a research perspective, we anticipate that it will enable the systematic quantification and mitigation of 3D-RT biases of imagery-derived cloud-aerosol radiative effects.

https://doi.org/10.5194/amt-2022-143
Preprint. Discussion started: 29 June 2022

Atmospheric Measurement Techniques Discussions

Appendix A

A1. Cloud Detection/Identification

Cloudy pixels are identified through a simple thresholding method based on the red, green, and blue channels of MODIS. When the radiance values of the red, green, and blue channels of a pixel are all greater than the corresponding median value, the pixel is considered as cloudy, as illustrated by the following equation

$$\textbf{If} \quad \begin{matrix} Red > Median(Red)\ \& \\ Blue > Median(Blue)\ \& \\ Green > Median(Green) \end{matrix} \quad \begin{cases} \textbf{Yes}, \text{cloudy} \\ \textbf{No}, \text{clear sky} \end{cases} \tag{A1}$$

Note that this only works for partially cloud-covered scenes, and may lead to false positives if there is brightness contrast from objects other than clouds. This method was specifically applied for the cases in this paper and should be changed as appropriate for future applications.

A2. Two-Stream Approximation

The two-stream approximation of the reflectance R is calculated using Eq. D2 from Chen et al. (2021), as follows:

$$R = \frac{\tau + \alpha \cdot \left(\frac{2\mu}{(1-g)\cdot(1-\alpha)}\right)}{\tau + \left(\frac{2\mu}{(1-g)\cdot(1-\alpha)}\right)} \tag{A2}$$

where τ is the cloud optical thickness, α is the surface albedo, μ is the cosine of the solar zenith angle, and g is the asymmetry parameter. A value of 0.85 is assumed for g. The domain average of the solar zenith angle and surface albedo are calculated and used for estimating μ and α. Then, for a range of τ, we calculated the R and obtained the relationship of $R(\tau)$. For those cloudy pixels identified through A1, the inverse relationship of $\tau(R)$ is then used for estimating τ at any given R. Note that this approach does not take into account any cloud reflectance anisotropies.

Appendix B

B1. Parallax Correction

From the satellite's view, the clouds (especially high clouds) will be placed at inaccurate locations on the surface, which have shifted from their actual locations due to the parallax effect. We followed simply trigonometry to correct for it, as follows:

Longitude correction (positive from west to east):

https://doi.org/10.5194/amt-2022-143
Preprint. Discussion started: 29 June 2022

Atmospheric Measurement Techniques Discussions

$$\delta lon = \frac{(z_{cld} - z_{sfc}) \cdot \tan(\theta) \cdot \sin(\phi)}{\pi \cdot R_{Earth}} \times 180° \quad \text{(B1)}$$

Latitude correction (positive from south to north):

$$\delta lat = \frac{(z_{cld} - z_{sfc}) \cdot \tan(\theta) \cdot \cos(\phi)}{\pi \cdot R_{Earth}} \times 180° \quad \text{(B2)}$$

where $(lon_{sat}, lat_{sat}, z_{sat})$ is the satellite location and θ and ϕ (0º at north, positive clockwise) are the sensor viewing zenith and azimuth angles. z_{cld} and z_{sfc} are the cloud top height and the surface height. R_{Earth} is the radius of the Earth. Figure A1 shows an illustration of parallax correction for the black-boxed cloud field in Figure 2.

B2. Wind Correction

The wind correction aims at correcting the movement of clouds when advected by the wind between two different satellites' overpasses.

Longitude correction (positive from west to east):

$$\delta lon = \frac{\bar{u} \cdot \delta t}{\pi \cdot R_{Earth}} \times 180° \quad \text{(B3)}$$

Latitude correction (positive from south to north):

$$\delta lat = \frac{\bar{v} \cdot \delta t}{\pi \cdot R_{Earth}} \times 180° \quad \text{(B4)}$$

where $\bar{u}$ and $\bar{v}$ are the domain-averaged 10 m zonal and meridional wind speeds, and δt is the time difference between two different satellites that fly on the same orbit. Figure A1 shows the cloud location after applying the parallax (Appendix B1) and wind correction for the cloud field in the black box from Figure 2.

https://doi.org/10.5194/amt-2022-143
Preprint. Discussion started: 29 June 2022

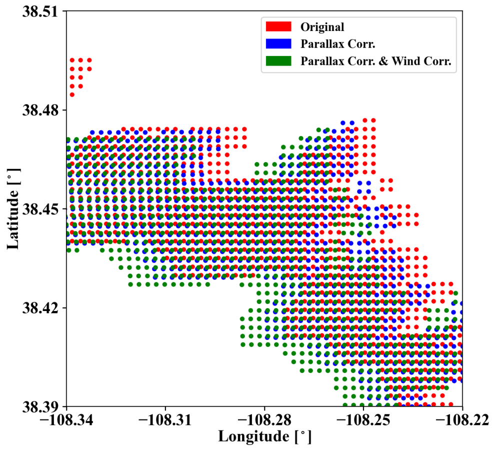

Figure A1. An illustration of correcting cloud location (red) for parallax effect (blue) and wind effect (green) for the black-boxed cloud field in Figure 2.

Acknowledgement

The aircraft all-sky camera was radiometrically calibrated by the U.S. Naval Research Laboratory.

References

Anderson, G. P., Clough, S. A., Kneizys, F. X., Chetwynd, J. H., and Shettle, E. P.: AFGL atmospheric constituent profiles (0–120 km), Tech. Rep. AFGL-TR-86–0110, Air Force Geophys. Lab., Hanscom Air Force Base, Bedford, Massachusetts, U.S.A., 1986.

Barker, H. and Liu, D.: Inferring optical depth of broken clouds from Landsat data, J. Climate, 8, 2620–2630, 1995.

Barker, H. W., Jerg, M. P., Wehr, T., Kato, S., Donovan, D. P., and Hogan, R. J.: A 3D cloud construction algorithm for the EarthCARE satellite mission, Q. J. Roy. Meteor. Soc., 137, 1042– 1058, https://doi.org/10.1002/qj.824, 2011.

Barker, H. W., Kato, S., and Wehr, T.: Computation of solar radiative fluxes by 1-D and 3-D methods using cloudy atmospheres inferred from A-train satellite data, Surv. Geophys., 33, 657–676, 2012.

Crisp, D.: Measuring Atmospheric Carbon Dioxide from Space with the Orbiting Carbon Observatory-2 (OCO-2), P. Soc. Photo.-Opt. Ins., 9607, 960702, https://doi.org/10.1117/12.2187291, 2015.

Coddington, O., Schmidt, K. S., Pilewskie, P., Gore, W. J., Bergstrom, R., Roman, M., Redemann, J., Russell, P. B., Liu, J., and Schaaf, C. C.: Aircraft measurements of spectral surface albedo and its consistency with ground-based and space-borne observations, J. Geophys. Res., 113, D17209, doi:10.1029/2008JD010089, 2008.

Deneke, H., Barrientos-Velasco, C., Bley, S., Hünerbein, A., Lenk, S., Macke, A., Meirink, J. F., Schroedter-Homscheidt, M., Senf, F., Wang, P., Werner, F., and Witthuhn, J.: Increasing the spatial resolution of cloud property retrievals from Meteosat SEVIRI by use of its high-resolution visible channel: implementation and examples, Atmos. Meas. Tech., 14, 5107–5126, https://doi.org/10.5194/amt-14-5107-2021, 2021.

Emde, C., Buras-Schnell, R., Kylling, A., Mayer, B., Gasteiger, J., Hamann, U., Kylling, J., Richter, B., Pause, C., Dowling, T., and Bugliaro, L.: The libRadtran software package for radiative transfer calculations (version 2.0.1), Geosci. Model Dev., 9, 1647–1672, https://doi.org/10.5194/gmd-9-1647-2016, 2016.

Evans, K. F.: The spherical harmonics discrete ordinate method for three-dimensional atmospheric radiative transfer, J. Atmos. Sci., 55, 429–446, 1998.

Gristey, J. J., Feingold, G., Glenn, I. B., Schmidt, K. S., and Chen, H.: Surface Solar Irradiance in

Continental Shallow Cumulus Fields: Observations and Large-Eddy Simulation, J. Atmos. Sci., 77, 1065–1080, https://doi.org/10.1175/JAS-D-19-0261.1, 2020a.

Gristey, J. J., Feingold, G., Glenn, I. B., Schmidt, K. S., and Chen, H.: On the Relationship Between Shallow Cumulus Cloud Field Properties and Surface Solar Irradiance, Geophysical Research Letters, 47, e2020GL090152, https://doi.org/10.1029/2020GL090152, 2020b.

Gristey, J. J., Feingold, G., Glenn, I. B., Schmidt, K. S., and Chen, H.: Influence of Aerosol Embedded in Shallow Cumulus Cloud Fields on the Surface Solar Irradiance, Journal of Geophysical Research: Atmospheres, 127, e2022JD036822, https://doi.org/10.1029/2022JD036822, 2022.

Heidinger, A. K., Foster, M. J., Walther, A., and Zhao, X.: The Pathfinder Atmospheres-Extended AVHRR climate dataset, B. Am. Meteorol. Soc., 95, 909–922, https://doi.org/10.1175/BAMS-D-12-00246.1, 2014.

Illingworth, A. J., Barker, H. W., Beljaars, A., Chepfer, H., Delanoe, J., Domenech, C., Donovan, D. P., Fukuda, S., Hirakata, M., Hogan, R. J., Huenerbein, A., Kollias, P., Kubota, T., Nakajima, T., Nakajima, T. Y., Nishizawa, T., Ohno, Y., Okamoto, H., Oki, R., Sato, K., Satoh, M., Wandinger, U., Wehr, T., and van Zadelhoff, G.: The EarthCARE Satellite: the next step forward in global measurements of clouds, aerosols, precipitation and radiation, B. Am. Meteorol. Soc, 96, 1311–1332, https://doi.org/10.1175/BAMS-D-12-00227.1, 2015.

Iwabuchi, H.: Efficient Monte Carlo methods for radiative transfer modeling, J. Atmos. Sci., 63, 2324–2339, 2006.

Kindel, B. C., Schmidt, K. S., Pilewskie, P., Baum, B. A., Yang, P., and Platnick, S.: Observations and modeling of ice cloud shortwave spectral albedo during the Tropical Composition, Cloud and Climate Coupling Experiment (TC^{4}), J. Geophys. Res., 115, D00J18, doi:10.1029/2009JD013127, 2010.

King, M., and Platnick, S.: The Earth Observing System (EOS), Comprehensive Remote Sensing, 7, 26, doi:10.1016/b978-0-12-409548-9.10312-4, 2018.

Levis, A., Schechner, Y. Y., Davis, A. B., and Loveridge, J.: Multi-View Polarimetric Scattering Cloud Tomography and Retrieval of Droplet Size, Remote Sens., 12, 2831, https://doi.org/10.3390/rs12172831, 2020.

Li, J., Scinocca, J., Lazare, M., McFarlane, N., von Salzen, K., and Solheim, L.: Ocean Surface Albedo and Its Impact on Radiation Balance in Climate Models, J. Climate, 19, 6314–6333,

https://doi.org/10.5194/amt-2022-143
Preprint. Discussion started: 29 June 2022

2006.

Long, C. N., Bucholtz, A., Jonsson, H., Schmid, B., Vogelmann, A., and Wood, J.: A Method of Correcting for Tilt from Horizontal in Downwelling Shortwave Irradiance Measurements on Moving Platforms, The Open Atmospheric Science Journal, 4, 78–87, 2010.

Masuda, R., Iwabuchi, H., Schmidt, K. S., Damiani, A. and Kudo, R.: Retrieval of Cloud Optical Thickness from Sky-View Camera Images using a Deep Convolutional Neural Network based on Three-Dimensional Radiative Transfer, Remote Sensing, 11(17), 1962, doi:10.3390/rs11171962, 2019.

Marshak, A., Davis, A., Wiscombe, W., and Cahalan, R.: Radiative smoothing in fractal clouds, J. Geophys. Res., 100, 26247–26261, https://doi.org/10.1029/95JD02895, 1995.

Marshak, A., Wen, G., Coakley, J., Remer, L., Loeb, N. G., and Cahalan, R. F.: A simple model for the cloud adjacency effect and the apparent bluing of aerosols near clouds, J. Geophys. Res., 113, D14S17, https://doi.org/10.1029/2007JD009196, 2008.

Massie, S. T., Schmidt, K. S., Eldering, A., and Crisp, D.: Observational evidence of 3-D cloud effects in OCO-2 CO2 retrievals, J. Geophys. Res. Atmos., 122, 7064–7085, https://doi.org/10.1002/2016JD026111, 2017.

Mayer, B. and Kylling, A.: Technical note: The libRadtran software package for radiative transfer calculations – description and examples of use, Atmos. Chem. Phys., 5, 1855–1877, https://doi.org/10.5194/acp-5-1855-2005, 2005.

Mayer, B.: Radiative transfer in the cloudy atmosphere, EPJ Web of Conferences, 1, 75–99, doi:10.1140/epjconf/e2009-00912-1, 2009.

Mlawer, E. J., Taubman, S. J., Brown, P. D., Iacono, M. J., and Clough, S. A.: Radiative transfer for inhomogeneous atmospheres: RRTM, a validated correlated-k model for the longwave, J. Geophys. Res., 102, 16663–16682, 1997.

Nakajima, T. and King, M. D.: Determination of the optical thickness and effective particle radius of clouds from reflected solar radiation measurements. Part I: Theory, J. Atmos. Sci., 47, 1878–1893, 1990.

Nataraja, V., Schmidt, S., Chen, H., Yamaguchi, T., Kazil, J., Feingold, G., Wolf, K., and Iwabuchi, H.: Segmentation-Based Multi-Pixel Cloud Optical Thickness Retrieval Using a Convolutional Neural Network, Atmos. Meas. Tech. Discuss. [preprint], https://doi.org/10.5194/amt-2022-45, in review, 2022.

https://doi.org/10.5194/amt-2022-143
Preprint. Discussion started: 29 June 2022

Atmospheric Measurement Techniques Discussions

Norgren, M. S., Wood, J., Schmidt, K. S., van Diedenhoven, B., Stamnes, S. A., Ziemba, L. D., Crosbie, E. C., Shook, M. A., Kittelman, A. S., LeBlanc, S. E., Broccardo, S., Freitag, S., and Reid, J. S.: Above-aircraft cirrus cloud and aerosol optical depth from hyperspectral irradiances measured by a total-diffuse radiometer, Atmos. Meas. Tech., 15, 1373–1394, https://doi.org/10.5194/amt-15-1373-2022, 2022.

Payne, V. H., Drouin, B. J., Oyafuso, F., Kuai, L., Fisher, B. M., Sung, K., Nemchicka, D., Crawford, T. J., Smyth, M., Crisp, D., Adkins, E., Hodges, J. T., Long, D. A., Mlawer, E. J., Merrelli, A., Lunny, E., and O'Dell, C. W.: Absorption coefficient (ABSCO) tables for the Orbiting Carbon Observatories: version 5.1, J. Quant. Spectrosc. Ra., 255, 1–16, https://doi.org/10.1016/j.jqsrt.2020.107217, 2020.

Pilewskie, P., Pommier, J., Bergstrom, R., Gore, W., Howard, S., Rabbette, M., Schmid, B., Hobbs, P. V., and Tsay, S. C.: Solar spectral radiative forcing during the Southern African Regional Science Initiative, J. Geophys. Res., 108, 8486, https://doi.org/10.1029/2002JD002411, 2003.

Pincus, R. and Evans, K. F.: Computational cost and accuracy in calculating three-dimensional radiative transfer: Results for new implementations of Monte Carlo and SHDOM, J. Atmos. Sci., 66, 3131–3146, 2009.

Platnick, S., King, M. D., Ackerman, S. A., Menzel, W. P., Baum, B. A., Riédi, J. C., and Frey, R. A.: The MODIS cloud products: Algorithms and examples from Terra, IEEE T. Geosci. Remote, 41, 459–473, 2003.

Reid, J. S., Maring, H. B., Narisma, G., van den Heever, S., DiGirolamo, L., Ferrare, R., Lawson, P., Mace, G. G., Simpas, J., Tanelli, S., Ziemba, L., van Diedenhoven, B., Bruintjes, R., Bucholtz, A., Cairns, B., Cambaliza, M. O., Chen, G., Diskin, G. S., Flynn, J. H., Hostetler, C. A., Holz, R. E., Lang, T. J., Schmidt, K. S., Smith, G., Sorooshian, A., Thompson, E. J., Thornhill, K. L., Trepte, C., Wang, J., Woods, S., Yoon, S., Alexandrov, M., Alverez, S., Amiot, C., Bennett, J. R., Brooks, M., Burton, S. P., Cayanan, E., Chen, H., Collow, A., Crosbie, E., DaSilva, A., DiGangi, J. P., Flagg, D. D., Freeman, S. W., Fu, D., Fukada, E., Hilario, M. R. A., Hong, Y., Hristova-Veleva, S. M., Kuehn, R., Kowch, R. S., Leung, G. R., Loveridge, J., Meyer, K., Miller, R., Montes, M. J., Moum, J. N., Nenes, T., Nesbit, S. W., Norgen, M., Novak, E., Rauber, R. M., Reid, E. A., Rutledge, S., Schlosser, J. S., Sekiyama, T. T., Shook, M. A., Sokolowsky, G. A., Stamnes, S. A., Sy, O. O., Tanaka, T. Y., Wasilewski, A., Xian, P., Xiao, Q., and Zavaleta, J.: The coupling between tropical meteorology, aerosol

Atmospheric Measurement Techniques Discussions

lifecycle, convection, and radiation, during the Clouds, Aerosol and Monsoon Processes Philippines Experiment (CAMP^{2}Ex), B. Am. Meteorol. Soc., *in review*, 2022.

Rothman, L., Jacquemart, D., Barbe, A., Chris Benner, D., Birk, M., Brown, L., Carleer, M., Chackerian, C., Chance, K., Coudert, L., Dana, V., Devi, V., Flaud, J.-M., Gamache, R., Gold- man, A., Hartmann, J.-M., Jucks, K., Maki, A., Mandin, J.- Y., Massie, S., Orphal, J., Perrin, A., Rinsland, C., Smith, M., Tennyson, J., Tolchenov, R., Toth, R., Vander Auwera, J., Varanasi, P., and Wagner, G.: The HITRAN 2004 molecular spectroscopic database, J. Quant. Spectrosc. Ra., 96, 139–204, https://doi.org/10.1016/j.jqsrt.2004.10.008, 2005.

Schmidt, K. S., Pilewskie, P., Platnick, S., Wind, G., Yang, P., and Wendisch, M.: Comparing irradiance fields derived from Moderate Resolution Imaging Spectroradiometer air- borne simulator cirrus cloud retrievals with solar spectral flux radiometer measurements, J. Geophys. Res., 112, D24206, doi:10.1029/2007JD008711, 2007.

Schmidt, S., Pilewskie, P., Mayer, B., Wendisch, M., Kindel, B., Platnick, S., King, M. D., Wind, G., Arnold, G. T., Tian, L., Heymsfield, G., and Kalesse, H.: Apparent absorption of solar spectral irradiance in heterogeneous ice clouds, J. Geophys. Res., 115, D00J22, https://doi.org/10.1029/2009JD013124, 2010.

Schmidt, S., Massie, S., Chen, H., Crisp, D., Kulawik, S., Chen, Y.-W., Merrelli, A., McDuffie, J., Iwabuchi, H.: Uncovering the Mechanism for Trace Gas Spectroscopy Biases in the Vicinity of Clouds With the OCO-2 3D Radiative Transfer Satellite Radiance Simulator, *to be submitted*, 2022.

Song, S., Schmidt, K. S., Pilewskie, P., King, M. D., Heidinger, A. K., Walther, A., Iwabuchi, H., Wind, G., and Coddington, O. M.: The Spectral Signature of Cloud Spatial Structure in Shortwave Irradiance, Atmos. Chem. Phys., 16, 13791–13806, https://doi.org/10.5194/acp-16-13791-2016, 2016.

Vermote, E. F., Roger, J. C., and Ray J. P.: MODIS Surface Reflectance User's Guide, MODIS Land Surface Reflectance Science Computing Facility, Version 1.4, 1-35, 2015.

Wood, J., Smyth, T. J., and Estellés, V.: Autonomous marine hyperspectral radiometers for determining solar irradiances and aerosol optical properties, Atmos. Meas. Tech., 10, 1723–1737, https://doi.org/10.5194/amt-10-1723-2017, 2017.